

Synthesis of clathrate cerium superhydride CeH₉ below 100 GPa with atomic hydrogen sublattice

Nilesh P. Salke¹, M. Mahdi Davari Esfahani², Youjun Zhang^{3,1}, Ivan A. Kruglov^{4,5}, Jianshi Zhou⁶,
Yaguo Wang⁶, Eran Greenberg⁷, Vitali B. Prakapenka⁷, Artem R. Oganov^{8,4,9,*}, Jung-Fu Lin^{10,*}

¹Center for High Pressure Science & Technology Advanced Research (HPSTAR), Shanghai, 201203, China

²Department of Geosciences, Center for Materials by Design, and Institute for Advanced Computational Science, State University of New York, Stony Brook, New York 11794-2100, USA

³Institute of Atomic and Molecular Physics, Sichuan University, Chengdu 610065, China

⁴Department of Problems of Physics and Energetics, Moscow Institute of Physics and Technology, 9 Institutskiy Lane, Dolgoprudny City, Moscow Region 141700, Russia

⁵Dukhov Research Institute of Automatics (VNIIA), Moscow 127055, Russia

⁶Department of Mechanical Engineering, The University of Texas at Austin, Austin, Texas 78712, USA

⁷Center for Advanced Radiation Sources, University of Chicago, Illinois, 60637, USA

⁸Skolkovo Institute of Science and Technology, Skolkovo Innovation Center, 3 Nobel Street, Moscow 143026, Russia

⁹International Center for Materials Design, Northwestern Polytechnical University, Xi'an 710072, China

¹⁰Department of Geological Sciences, The University of Texas at Austin, Austin, Texas 78712, USA

*Corresponding author: Jung-Fu Lin (afu@jsg.utexas.edu)

*Corresponding author: Artem R. Oganov (artem.oganov@stonybrook.edu)

Abstract

Hydrogen-rich superhydrides are believed to be very promising high- T_c superconductors as they are expected to mimic characteristics of metallic hydrogen. Recent experiments discovered superhydrides at very high pressures, e.g. FeH₅ at 130 GPa and LaH₁₀ at 170 GPa. With the motivation of discovering new hydrogen-rich high- T_c superconductors at lowest possible pressure, here we report the prediction and experimental synthesis of cerium superhydride CeH₉ below 100 GPa in the laser-heated diamond anvil cell. Ab-initio calculations were carried to evaluate the detailed chemistry of the Ce-H system and to understand the structure, stability and superconductivity of CeH₉. CeH₉ crystallizes in a $P6_3/mmc$ clathrate structure with a substantially dense 3-dimensional hydrogen sublattice at 100 GPa. These findings shed a new light on the search for superhydrides in close proximity with atomic hydrogen within a feasible pressure range. Discovery of superhydride CeH₉ provides a practical platform to further investigate and understand conventional superconductivity in hydrogen rich superhydrides.

Main text

Metallization of hydrogen under high pressure has been a topic of great scientific interest in the past few decades mainly due to expectations of room-temperature superconductivity¹⁻⁷. Hydrogen is expected to become metallic under high pressure above 400 GPa⁷⁻⁹. But achieving such pressures is very challenging in diamond anvil cell experiments, mainly due to diamond failure and lack of a reliable probe on the tiny sample volumes at such high pressures. Meanwhile hydrogen-rich hydrides are also expected to achieve high- T_c superconductivity perhaps at a much lower pressure than that of required for metallic hydrogen¹⁰⁻¹². Hydrides and metallic hydrogen are expected to be conventional superconductors due to the presence of hydrogen. For conventional superconductivity, high phonon frequency, strong electron-phonon coupling and high density of states at the Fermi level are the essential conditions for superconductivity with Cooper pairs mediated by electron-phonon interaction¹³. Existence of hydrogen in hydride sublattice satisfies all these conditions as the low mass of hydrogen results in high phonon frequency, covalent bonding is favourable for strong electron-phonon coupling, and metallization under high pressure can result in high electronic density of states at the Fermi level¹⁰. Within this view the remarkable prediction and experimental confirmation of superconductivity at a record high T_c of 203 K under pressure of 150 GPa in H₃S makes sense^{14,15}. The discovery of superconductivity in H₃S has given hopes to achieve room-temperature superconductivity in hydrogen-rich systems under high pressure.

Hydrogen readily reacts with most elements to form binary hydrides.^{16,17} Several hydrogenic motifs such as H^{δ-}, H₂^{δ-}, H₃⁻, H₃⁺, H₄⁻ and H₅⁺, and infinite chains, layers, frameworks were predicted to occur in high-pressure hydrides¹⁸⁻²⁰. 1-D hydrogen chains and 3-D clathrate structures with hydrogen cage were predicted and found to be good candidates for high T_c superconductivity¹⁸. H₃S with highest T_c of 203 K has body centered cubic structure which can also be visualized as sulphur atom surrounded by 3-dimensional hydrogen cage. Hydrides possessing H₂-units are not prone to have high T_c as they tend to have low densities of states at the Fermi level²¹. Recent theoretical predictions have reported several systems with unusually high hydrogen content, termed as polyhydrides/superhydrides, to become stable under high pressure and to have very high T_c under pressure²⁰⁻²⁷. Notably CaH₆²², MgH₆²⁴, YH₆²⁵, YH₉²¹, YH₁₀^{21,26}, LaH₁₀²⁶, AcH₁₀ and AcH₁₆²⁷ were predicted to have T_c above 235 K. Most of the phases with T_c close to room temperature are predicted to have a clathrate structure with hydrogen forming a cage around metal atom (M). In MH_6 , MH_9 and MH_{10} compounds,

metal atoms are located within H_{24} , H_{29} and H_{32} cages respectively^{21,22,25,26}. However, it is essential to know the experimental pressure-temperature condition to stabilize a hydride before carrying out the further electrical or magnetic measurement to verify the superconductivity. Recently, a handful of experiments were reported to synthesize new superhydrides under pressure, particularly FeH_5 at 130 GPa²⁸, LaH_{10} at 170 GPa²⁹, UH_7 , UH_8 and UH_9 above 37 GPa³⁰. There were also experimental reports about synthesis of new and unusual hydrides under pressure, such as LiH_6 ³¹, NaH_7 ³², $Xe(H_2)_7$ ³³ and $HI(H_2)_{13}$ ³⁴ with H_2 -like molecular units. Synthesis of FeH_5 and LaH_{10} without any H_2 -like unit is very intriguing. Following to the experimental synthesis of LaH_{10} , recently the experimental T_c of 260 K at 190 GPa and 215 K at 150 GPa is claimed for LaH_{10} by two different research groups by electrical conductivity measurement^{35,36}, if proven it would be a new record. However, there is a huge discrepancy in the claimed T_c by two independent measurement, mainly because the very high pressure of 170 GPa involved in the synthesis of LaH_{10} . At such pressure the verification of T_c becomes challenging task. Interestingly, FeH_5 with layered structured consisted 2-dimensional atomic hydrogen slabs. Also, nearest H-H distance in FeH_5 was reported to be ~ 1.336 Å at ~ 100 GPa²⁸, whereas for LaH_{10} it was ~ 1.196 Å at ~ 120 GPa²⁹. LaH_{10} was claimed as closest analogue to solid atomic metallic hydrogen based on nearest H-H distance.²⁹ But the pressure required to stabilize FeH_5 and LaH_{10} phases was 130 and 170 GPa, respectively^{28,29}, which is relatively high. It would be desirable to get hydrogen-rich phases with the lowest possible pressure for further experimental verifications and realistic technological application. Synthesis of superhydrides at lower pressures would give an opportunity to further investigate the nature of superconductivity and atomic hydrogen by other techniques for an in-depth understanding. Studies on the synthesis path and structure of superhydrides also help to build a deeper understanding of hydride chemistry. Besides superconductivity, hydrides are also very important as hydrogen storage materials for next generation energy related applications³⁷. Recently, Peng et al. (2017) predicted that hydrogen-rich CeH_9 with $P6_3/mmc$ structure becomes stable at a relatively low pressure of 100 GPa²¹, which by itself is very interesting although their estimated superconducting T_c was relatively low, < 56 K. We have carefully studied the Ce-H system in order to understand the crystal chemistry and to seek for superconductivity with, much higher T_c values.

Here we report the successful synthesis of cerium superhydride CeH_9 below 100 GPa. Using evolutionary variable-composition searches, whole compositional space of the Ce-H system explored in a single simulation. We predicted phase stability and superconducting

properties of high-pressure cerium superhydrides. Rich chemistry of cerium hydrides manifests itself in numerous stable compounds, including the experimentally synthesized CeH_3 and superhydrides CeH_9 . We have carried out a direct elemental reaction between cerium and hydrogen using a laser-heated diamond anvil cell (DAC) coupled with synchrotron x-ray diffraction (XRD). It is found that heating plays an essential role in the formation of Ce-H phases at high pressures. Analysis of XRD results in combination with *ab initio* calculations shows that CeH_9 crystallizes in a clathrate structure with space group $P6_3/mmc$ above 80 GPa. Each cerium atom is enclosed within a cage of H_{29} in which hydrogen atoms are bonded covalently. Besides this, a previously unknown $Pm\bar{3}n$ structured CeH_3 ($\beta\text{-UH}_3$ type³⁸) was synthesized at 36 GPa with laser heating. The detailed first-principles investigation of stability, structural, electronic and superconducting properties of experimentally synthesized hydrogen-rich phase was carried out. We studied, specifically electron-phonon interaction of $P6_3/mmc$ - CeH_9 and predict that the CeH_9 is a high temperature superconductor with $T_c = 117$ K at 200 GPa.

Results

Synthesis of various Ce-H phases. In our experiment, various phases of the Ce-H system such as CeH_x ($x = 2, 2.5, 3$ and 9) were synthesized successfully at high pressures. Initially, the cerium sample and hydrogen gas were loaded into the sample chamber of the DAC and were kept at 9 GPa. A small piece of gold also was loaded along with sample to calibrate pressure. At 9 GPa and ambient temperature, we found that cerium and hydrogen reacted in the sample chamber which resulted in the formation of a cerium hydride compound as shown by the XRD pattern in Fig. 1a. The corresponding XRD image is shown in supplementary Fig. S1a. All the peaks observed at 9 GPa could be indexed with the $Fm\bar{3}m$ phase of CeH_2 . The $Fm\bar{3}m$ phase of CeH_2 persisted up to 33 GPa (supplementary Fig. S1b). Le Bail refinements were carried to extract lattice parameters of the CeH_2 phase (supplementary Fig. S1c). The lattice parameters of CeH_2 at 9 GPa and 33 GPa were determined as $a = 5.370(1)$ and $a = 5.011(2)$ Å respectively. Pressure dependence of the unit cell volume of CeH_2 was fitted with a third-order Birch-Murnaghan equation of state (EOS) which yielded the fitting parameters such as unit cell volume at zero pressure $V_0 = 44(1)$ Å³/f.u., bulk modulus $K_0 = 45(6)$ GPa and first pressure derivative of bulk modulus $K_0' = 4$ (fixed) (supplementary Fig. S1d). Pressurization of CeH_2 up to 33 GPa did not result in any changes in crystal structure. However, microsecond pulsed laser heating of ~ 2000 K carried at 33 GPa resulted in obvious structural changes

(supplementary Fig. S2a). The XRD pattern at 36 GPa obtained after laser heating is shown in Fig. 1b, and the corresponding XRD image is shown in supplementary Fig. S2b. The integrated XRD pattern at 36 GPa was found to be of cubic CeH₃ with $Pm\bar{3}n$ isomorphous to β -UH₃ (β - $Pm\bar{3}n$)³⁸. This high-pressure phase of CeH₃ with β - $Pm\bar{3}n$ structure has also been predicted in our evolutionary searches to be the energetically favourable phase below 10 GPa and is 32 meV/atom higher in enthalpy than the most favourable CeH₃ at the synthesized pressure of 36 GPa (supplementary Fig. S3). β -UH₃ type $Pm\bar{3}n$ -CeH₃ is being reported for the first time here. The experimental lattice parameters of the β - $Pm\bar{3}n$ phase at 36 GPa are $a = 6.2788(3)$ Å. In β - $Pm\bar{3}n$ structure of CeH₃, cerium atoms occupy 2a (0, 0, 0) and 6c (1/4, 0, 1/2) Wyckoff positions³⁸. Unfortunately, very low x-ray scattering factor of hydrogen atom did not allow us to determine the exact position of hydrogen atoms in CeH₃ unit cell from the experimental XRD data. Theoretical calculations yielded the Wyckoff position for the hydrogen atoms as 24K (0, 0.1580, 0.6935) at 35 GPa with lattice parameter $a = 6.2471$ Å, which is highly consistent with the experimental value of β - $Pm\bar{3}n$ -CeH₃ observed at 36 GPa. The β - $Pm\bar{3}n$ phase of CeH₃ proved stable with further compression up to 80 GPa and also sustained laser heating at an intermediate pressure of 60 GPa (supplementary Fig. S2a), which agrees with our predictions. A third-order Birch-Murnaghan EOS was used to fit the P - V data of CeH₃ (see supplementary Fig. S2d), fitting parameters are $V_0 = 39.7(4)$ Å³/f. u., $K_0 = 86(4)$ GPa and $K_0' = 4$ (fixed).

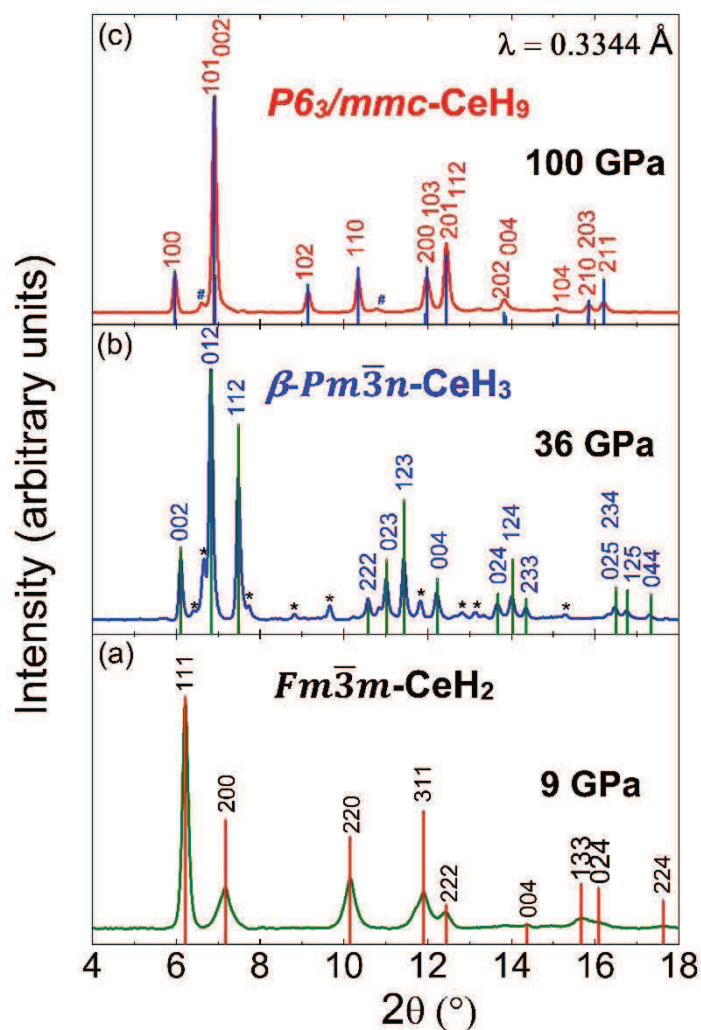


Figure 1: Representative integrated XRD patterns of high-pressure phases in Ce-H system up to 100 GPa. Typical XRD patterns of (a) CeH₂, (b) CeH₃, and (c) CeH₉ obtained at 9, 36 and 100 GPa of pressure respectively. Vertical lines indicate the indexing with calculated intensity for respective crystal structure. CeH₂, CeH₃ and CeH₉ crystallize in space group $Fm\bar{3}m$, $Pm\bar{3}n$ (β -UH₃ type) and $P6_3/mmc$ respectively. Unidentified weak peaks in (b) and (c) are marked with * and #, respectively. These additional peaks could not be identified or indexed with any of the known or predicted phases of Ce³⁹ or CeH_x²¹, as well as cerium oxides^{40,41}.

Several cycles of pulse laser heating with 1 μ s pulse width at a repetition rate of 10kHz for a total heating duration of a few seconds each cycle was used to laser heat the sample assemblage to approximately 1700 K at 80 GPa that resulted in the emergence of new peaks (supplementary Fig. S4). These new diffraction peaks were indexed to be (101) and (002) of clathrate hexagonal phase of CeH₉ (see supplementary Fig. S4 and Figs. 1c and 2) predicted by our evolutionary search. With further pressurization the relative intensity of the (101) and (002) peaks of CeH₉ phase increased (supplementary Fig. S4). Although most of the peaks of CeH₃ phase were present, the intensity of the CeH₉ peaks became prominent and increased with pressure (supplementary Fig. S4). Several further cycles of laser heating at 88 GPa

(supplementary Fig. S4) and 98 GPa improved the intensity of the hexagonal CeH₉ phase, as shown in Fig. 1c. A Rietveld refinement plot for the CeH₉ phase at 100 GPa is shown in Fig. 2a with the corresponding XRD image as an inset. CeH₉ crystallizes in the *P6₃/mmc* space group with lattice parameters $a = 3.7110(3)$ and $c = 5.5429(7)$ Å at 100 GPa. Cerium atoms occupy the Wyckoff position 2d (2/3, 1/3, 1/4) in a hexagonal unit cell. Theoretical calculations established positions of hydrogens to be 2b (0, 0, 1/4), 4f (1/3, 2/3, 0.1499) and 12k (0.1565, 0.8435, 0.4404) at 100 GPa. The crystal structure of CeH₉ is shown in Fig. 2b. The experimentally observed *P6₃/mmc* CeH₉ phase and its structural parameters are perfectly consistent with our calculations. Calculated EOS parameters for CeH₉ phase are as follows, $V_0 = 53.4(2)$ Å³/ f.u., $K_0 = 80.5(13)$ GPa and $K_0' = 4$ (fixed).

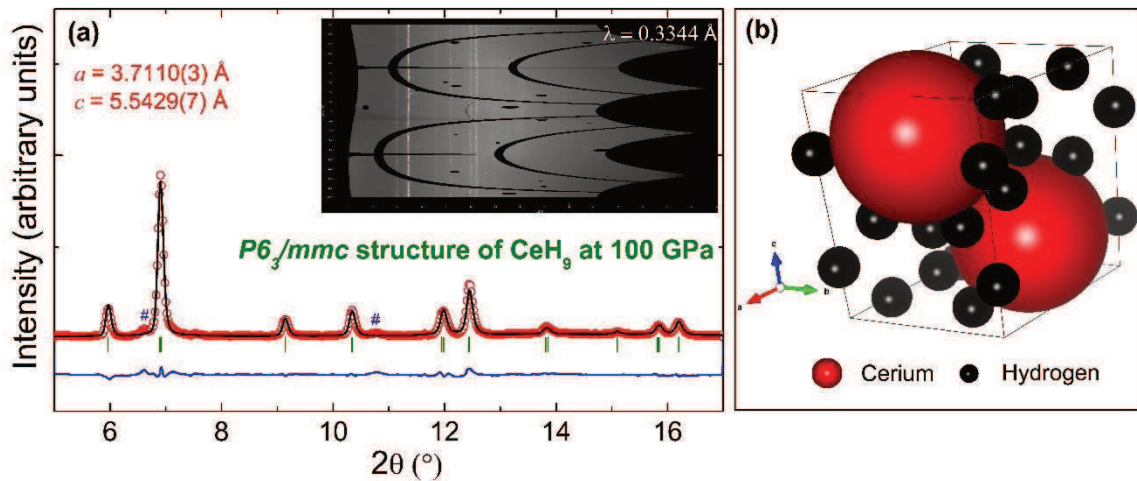


Figure 2: Rietveld refinement of the hexagonal CeH₉ in *P6₃/mmc* structure at 100 GPa. (a) Rietveld refinement plot of powder XRD data at 100 GPa. Red open circles: experimental data of CeH₉ in *P6₃/mmc* structure at 100 GPa; black line: model fit for the structure; green vertical lines: Bragg diffraction positions of the structure; blue line: residues. Reliability parameters for the Rietveld refinement are as follows (in %): $R_p = 14.5$, $R_{wp} = 18.4$, $R_{Bragg} = 8.05$. # represents unidentified weak peaks. Inset shows the Pilatus XRD image of corresponding powder XRD pattern with the incident x-ray wavelength of 0.3344 Å. (b) Crystal structure model of *P6₃/mmc* structured CeH₉. Red and black spheres represent cerium and hydrogen atoms respectively.

During the decompression cycle, the CeH₉ phase was observed to become unstable at pressures below 93 GPa (supplementary Fig. S5). Laser heating was also carried out during the decompression cycle at 79 and 54 GPa. Laser heating in decompression cycle did not show any precise changes in XRD pattern. Upon further decompression, the β -*Pm* $\bar{3}n$ -CeH₃ phase reappeared below 50 GPa (supplementary Fig. S5). Finally, after complete decompression, the β -*Pm* $\bar{3}n$ -CeH₃ phase was recovered at ambient conditions along with tetragonal Ce₂H₅ (supplementary Fig. S5). The *P-T* path for the formation and stability of various Ce-H phases, observed in our experiments, can be seen in Fig. S6.

Theoretical calculations and prediction of cerium hydrides. First-principles calculations were carried out to understand the detailed chemistry of the Ce-H system, dynamical stability, and structural and electronic band structures of experimentally synthesized superhydride phases. We performed variable-composition evolutionary searches at 0, 50, 100, 150, 200 and 250 GPa. The thermodynamic convex hull construction at different pressures is depicted in supplementary Fig S7. We predicted stable cerium hydrides and their stable structures at different pressure conditions, which are shown in the pressure-composition phase diagram in Fig. 3. Several compounds such as $I4/mmm$ -CeH₄, $P6_3mc$ -CeH₆, $P6_3mc$ -CeH₈, $P6_3/mmc$ -CeH₉ and $Fm\bar{3}m$ -CeH₁₀, were predicted, in addition to finding three known compounds CeH₂, Ce₂H₅. High-pressure phase of the CeH₃ was also predicted with space group $Pm\bar{3}n$, as shown in Fig. 3. Because of high concentration of hydrogen in hydrogen-rich hydrides, anharmonic effects might be important in determining the relative stability of hydrogen-rich phases, however, in our previous studies^{20,42}, we showed that quantum effects do not change the topology of the phase diagram, and quantitative effects are just moderate shifts in transition pressures. For example, the inclusion of ZPE lowers the formation enthalpies of $Ama2$ and $C2/m$ structures and shifts the transition pressure $Ama2 \rightarrow C2/m$ from 300 to 278 GPa⁴². Among the stable phases predicted, we have synthesized $Fm\bar{3}m$ -CeH₂, $I4_1md$ -Ce₂H₅ β - $Pm\bar{3}n$ -CeH₃ and $P6_3/mmc$ -CeH₉. Our pressure-composition phase diagram shows pressure ranges of stability for all the predicted phases along with experimentally known compounds. It clearly shows that higher pressures favour higher hydrogen content compounds, which is consistent with our experiment done at different pressure conditions. Previously known compounds $Fm\bar{3}m$ -CeH₂ and $I4_1md$ -Ce₂H₅ are predicted to be stable only below 8 and 1.5 GPa, respectively. Increase of pressure leads to the formation of $I4/mmm$ -CeH₄ above 32 GPa. CeH₆ and CeH₈ are stable in relatively narrow pressure ranges from 26 to 68 GPa, and 55 to 95 GPa, respectively and that is probably why they are not observed in our experiment. $P6_3/mmc$ -CeH₉ becomes stable at pressures above 78 GPa, which agrees with our high-pressure experiments where it was synthesized above 80 GPa. Detailed structural information on the predicted phases can be found in the supplementary Table S1. Among the predicted stable cerium hydrides, we focus our modelling on hydrogen-rich CeH₉, since a higher hydrogen to metal ratio in hydrides is expected to correlate with higher T_c superconductivity in hydrogen-rich hydrides¹¹.

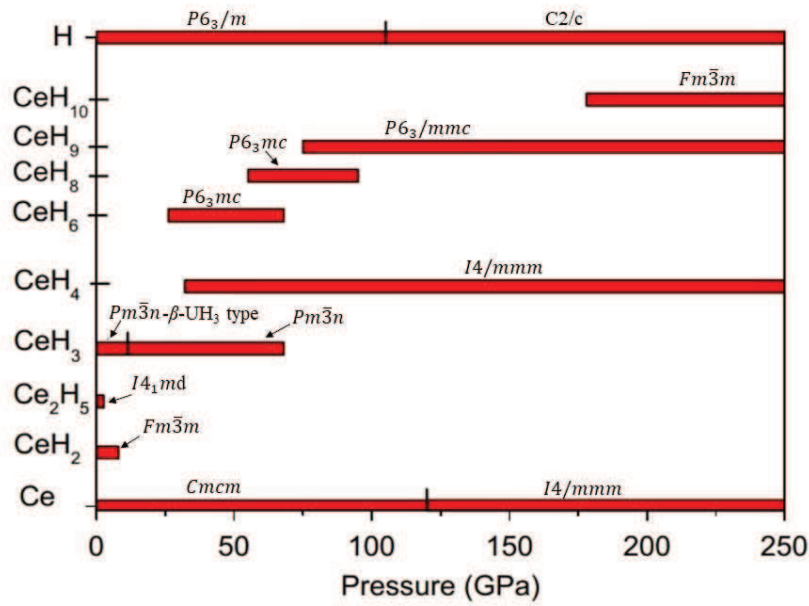


Figure 3: Pressure-composition phase diagram of theoretically predicted stable phases in the Ce-H system at high pressures. Red horizontal bars correspond to each Ce-H composition with a predicted crystal structure with its pressure range of stability calculated using the evolutionary structure search USPEX. The experimentally discovered *P6₃/mmc*-CeH₉ is predicted to be stable in the pressure range 78-250 GPa.

Discussion

Addition of hydrogen in metallic sublattice expands the unit cell volume. In most cases, rate of increase in volume is proportional to hydrogen content in hydride. In hydrides, expansion of volume with respect to pure metal volume were frequently used to establish the hydrogen content and stoichiometry²⁹. In order to ascertain the stoichiometry of high pressure superhydride phase observed above 80 GPa, we have compared the ideal mixture of Ce-H₂ solution with experimental volume per formula unit of CeH₃, CeH₉ and with theoretical EOS (see Fig. 4a). The curve representing ideal mixture of Ce and (7/2) H₂ lies well below the theoretical and experimental EOS of *P6₃/mmc*-CeH₉ in the pressure range 80 to 100 GPa. Whereas mixture of Ce and (8/2) H₂ partially overlaps with theoretical and experimental EOS of CeH₉. This indicates that the hexagonal phase observed above 80 GPa does not favour energetically CeH_x with $x < 8$ and can decompose into its elemental constituents or hydride with $x > 8$ and hydrogen. On the other hand, the curve representing an ideal mixture of Ce and (9/2) H₂ lies well above the theoretical and experimental EOS of CeH₉ in the pressure range 80 to 100 GPa. This observation clearly indicated that CeH₉ can be stabilized in the pressure range mentioned. From our theoretical calculations and energetic considerations, it clearly signifies that the hexagonal phase observed above 80 GPa with laser heating has the CeH₉ stoichiometry.

We can also see that there is a fair agreement between experimental volume and theoretical EOS results (Fig. 4a) for $P6_3/mmc$ -CeH₉ as well as β - $Pm\bar{3}n$ -CeH₃.

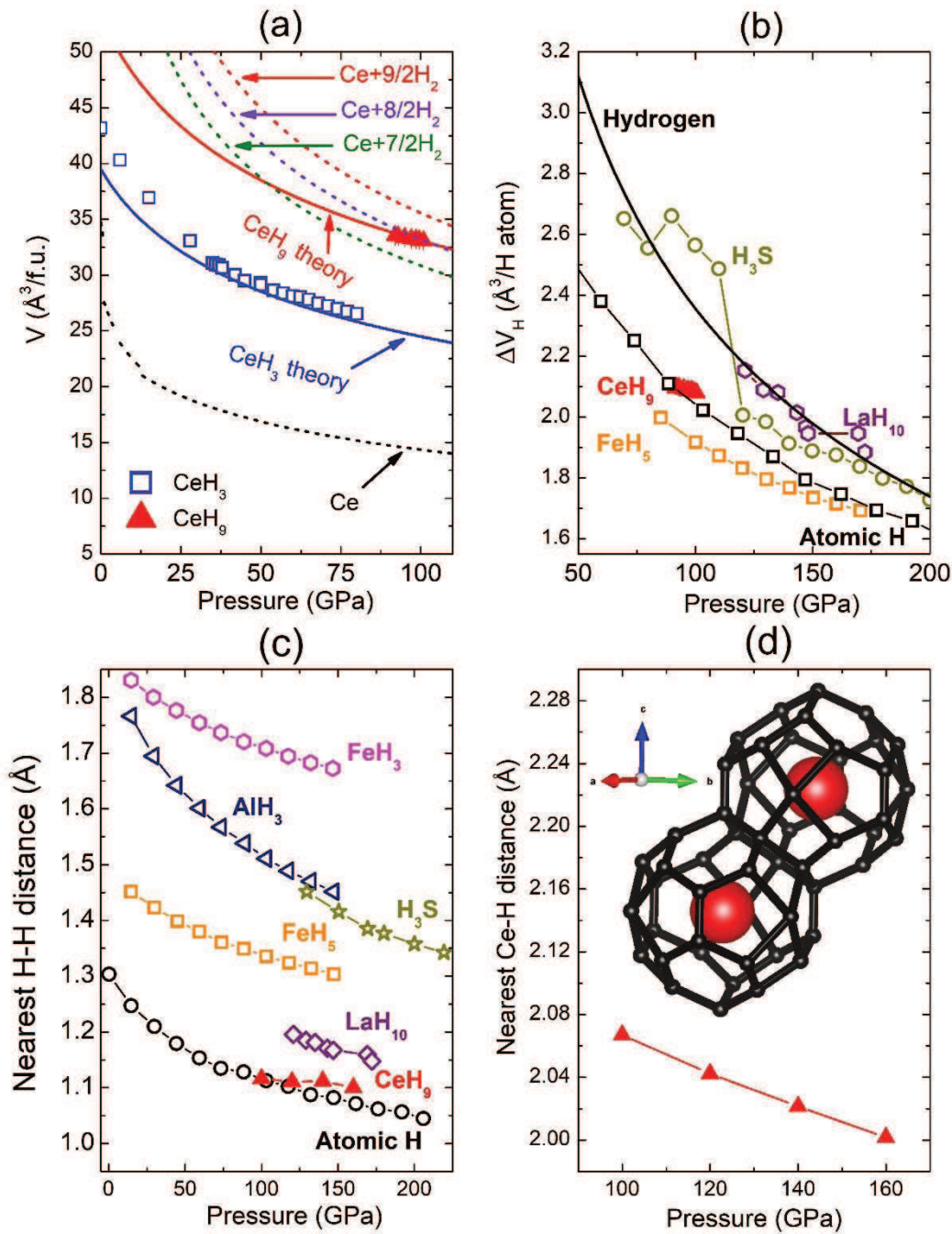


Figure 4: Effect of hydrogen on unit cell volume and nearest neighbour distances in various hydrides at high pressures. (a) Experimentally obtained volume per formula unit for CeH₃ and CeH₉ as a function of pressure. Theoretical EOS of CeH₃ and CeH₉ is plotted as blue and red lines, respectively. Black dashed line represents EOS of cerium metal.³⁹ Red, purple and green dashed curves represent ideal mixtures of Ce + (9/2)H₂, Ce + (8/2)H₂ and Ce + (7/2)H₂, respectively.^{39,43} (b) Volume expansion per hydrogen atom (ΔV_H) plotted against pressure for CeH₉, FeH₅²⁸, H₃S¹⁴, LaH₁₀²⁹, H₃⁴³ and atomic H₂ for comparison (c) Comparison of the pressure dependence of the nearest H-H distances for CeH₉, FeH₃⁴⁴, FeH₅²⁸, AlH₃⁴⁵, H₃S¹⁴, LaH₁₀²⁹ and atomic H₂.²⁸ (d) Nearest Ce-H distance for CeH₉ as a function of pressure. Inset shows Ce-H₂ clathrate cage in $P6_3/mmc$ structure. [Pressure dependent experimental data is at 300 K, whereas theoretical data is at 0 K]

In hydrides, hydrogen is pre-compressed in the vicinity of metal atoms. Hydrogen sublattice in hydrides is expected to be identical with atomic metallic hydrogen. So, we compared the volume expansion per hydrogen atom (ΔV_H) and nearest H-H distance in CeH₉ with simulated atomic metallic hydrogen phase extrapolated to lower pressure²⁸ and also with other reported hydrides as shown in Figs. 4b and 4c, respectively^{28,29,44,45}. The nearest Ce-H distance in $P6_3/mmc$ -CeH₉ is plotted in Fig. 4d. The inset of Fig. 4d shows the Ce-H₂₉ clathrate cage structure in which the H₂₉ cage is encircling a cerium atom. ΔV_H for CeH₉ is 2.09 Å³ at 100 GPa which is lower than that for a hydrogen atom, but larger by ~8% with respect to ΔV_H of layered FeH₅. ΔV_H for CeH₉ matches with volume of atomic metallic hydrogen around 100 GPa. Formation of CeH₉ can also be imagined as an absolute mixing of Ce and dense atomic metallic hydrogen. It indicates that hydrogen slab surrounding Ce atom is identical to dense atomic metallic hydrogen at a lower pressure. Nearest H-H distance in clathrate CeH₉ is 1.116 Å at 100 GPa, which is significantly longer than the H-H bond length (0.74 Å) in H₂ gas molecules but is significantly lower than in other hydrides such as AlH₃, FeH₃, FeH₅, H₃S and LaH₁₀ as can be seen in Fig. 4c. Surprisingly, the nearest H-H distance in CeH₉ almost overlaps with the H-H distance in atomic hydrogen and decreases very slowly with pressure. Among all the superhydrides, the nearest H-H distance observed in CeH₉ is remarkably short at 100 GPa and coincides with H-H distance of atomic metallic hydrogen. Among the reported hydrides, nearest H-H distance of CeH₉ is only second to the H-H distance (0.98 Å)²¹ for atomic metallic hydrogen at 500 GPa at which hydrogen is in a superconducting metallic state⁴⁶. Presence of strongly coupled hydrogen-dominant libration and stretch vibrations are the signatures of high- T_c in hydrogen-rich materials⁴⁷. Weak H-H interactions with preferred bond distances between 1.2 to 1.3 Å, the stretching and bending vibrations becomes indistinguishable, due to which all H vibrations contribute in the strong electron-phonon coupling process, eventually contributing to enhance the T_c in hydrides⁴⁷. At 100 GPa the nearest Ce-H distance is ~2.07 Å and it decreases with pressure. It is noteworthy that the clathrate structures predicted in the literature for rare earth (RE) hydrides REH₆, REH₉ and REH₁₀ have H₂₄, H₂₉ and H₃₀ cages surrounding the metal atom²¹. Among these cages, The H₂₉ cage has the smallest volume per formula unit for YH₉²¹. Clathrate H₂₉ cage in CeH₉ surrounding the Ce atom is almost 1.1 Å thick along the a - and b -axis, while it is 0.9 Å thick along c - axis at 100 GPa⁴⁸, whereas thickness of clathrate cage in LaH₁₀ is 0.9 Å²⁹. Clathrate structured CeH₉ can be visualized as 3-dimensional atomic metallic hydrogen encapsulating Ce atoms (inset of Fig. 4d). Covalently bonded hydrogen sublattice in CeH₉ with bond length and ΔV_H similar to atomic metallic hydrogen is likely to have density similar to that for atomic

hydrogen slab at 100 GPa. Hence $P6_3/mmc$ -CeH₉ will be a good platform to investigate H-H properties to understand atomic metallic hydrogen. Recently, Carbotte et al, proposed a new technique to investigate superconductivity in high pressure hydrides and hydrogen based on optical properties, without four probes.⁴⁹ Superconductivity in $P6_3/mmc$ -CeH₉ can also be evaluated using this optical technique.

Fig. 5a shows calculated electronic band structures of CeH₉ at 150 GPa. From Fig. 5a, it can be seen that CeH₉ is metallic and features numerous flat bands above the Fermi level. Noticeable density of electronic states at the Fermi level 0.73 states/eV/f.u., which is 1.4 times higher than that of previously found H₃S¹⁴ and comparable to that of recently synthesized LaH₁₀²⁹ at an optimal pressure of 200 GPa, is a good sign for getting high-temperature superconductivity. (see supplementary Fig. S8 and Table S2). The main contributors to $N(E_f)$ are Ce-4f and H-1s orbitals, however, only those electrons that are coupled strongly to phonons are important. High frequency phonons are mainly related to H vibrations, owing to its light mass, which makes the largest contribution to the electron-phonon coupling constant. Analysis of electron localization function (ELF) shows a moderate ELF value 0.64 between H atoms within the unit, suggesting weak covalent interaction, which forms a 3D hydrogen network i.e., H₂₉ cage consisting of H₄, H₅ and H₆ rings. Very low ELF value between Ce and H indicates that no bonds were present between the Ce and H atoms (supplementary Fig. S9).

We performed phonon calculations in the thermodynamic stability range of CeH₉ i.e., above 80 GPa. Lattice dynamics calculations indicate that the $P6_3/mmc$ -CeH₉ phase is dynamically stable at 150 GPa (Fig. 5b). Selected vibrational mode displacements of the $P6_3/mmc$ -CeH₉ at the H- and K-point from the structure relaxed at 150 GPa (see supplementary Fig. S10). However, at lower pressures, e.g., 120 GPa, calculations show that some phonon modes become imaginary along the H- and K-points ($[-1/3, 2/3, 1/2]$ and $[-1/3, 2/3, 0]$, respectively) (supplementary Figs. S10). To resolve the soft modes of the lattice, we used generalized evolutionary metadynamics (GEM)⁵⁰, in which large displacements along the softest mode eigenvectors are used to equilibrate the system. This hybrid technique is implemented in USPEX and was successfully applied to boron and silicon and found numerous energetically competitive configurations⁵⁰. We used supercells up to index 4 i.e., 80 atoms per cell. Using GEM, we found a stable structure with $C2/c$ symmetry (Supplementary Fig. S11), which is a subgroup of $P6_3/mmc$ symmetry. Electron-phonon coupling (EPC) calculations revealed that $P6_3/mmc$ -CeH₉ is a high temperature superconductor. Using the Allen-Dynes

modified McMillan equation (Eq. 1), we estimated the superconducting transition temperature (T_c) to be 117 K at 200 GPa, when using the commonly accepted value of 0.10 for the Coulomb pseudopotential μ^* . In $P6_3/mmc$, the resulting electron-phonon coupling coefficient λ is 2.30 at 200 GPa, which is higher than that of H_3S , $\lambda = 2.19$ at 200 GPa¹⁴. Since cerium atoms are heavy, the logarithmic average phonon frequency ($\omega_{\log} = 740$ K) is lower compared with that of H_3S ($\omega_{\log} = 1335$ K), which results in a lower T_c value of 117 K. The T_c of CeH_9 has a lower value of 75 K at 100 GPa for $C2/c$ structure. Logarithmic average phonon frequency ω_{\log} of $C2/c$ phase has a lower value 662 K. However, our results indicate that lower T_c value is mainly related to the lower electron-phonon coupling coefficient $\lambda = 1.48$. In contrast, earlier report by Peng et. al. (2017) predicted a T_c value of lower than 56 K at 100 GPa for CeH_9 phase with $P6_3/mmc$ structure²¹. However, our phonon calculations indicate instability of $P6_3/mmc$ phase below 120 GPa (see supplementary Fig. S10). So, our systematically carried studies estimate comparatively higher T_c of 75 K for CeH_9 at 100 GPa for the dynamically stable $C2/c$ structure. Furthermore, we have tabulated the ω_{\log} , λ and T_c value of CeH_9 along with recently predicted other superhydrides of La-H, Y-H, U-H, Ac-H and Th-H system for comparison, as shown in Table S3. Phonon dispersions curves, phonon density of states, the Eliashberg spectral function $\alpha^2F(\omega)$, and the EPC parameter λ as a function of frequency are calculated and shown in supplementary Figs. S12 and S13 for $C2/c$ and $P6_3/mmc$ - CeH_9 at 100 and 200 GPa, respectively. It is known that quantum effects can impact the calculated superconducting transition temperatures, however in the case of strong anharmonic H_3S (SG $Im\bar{3}m$), the inclusion of anharmonic correction, lowered the T_c from its harmonic 204 K value¹⁴ only to 194 K⁵¹ at 200 GPa, and both are close to the reported experiment T_c at 200 GPa¹⁵, although the transition pressures shift is considerably large^{14,52}.

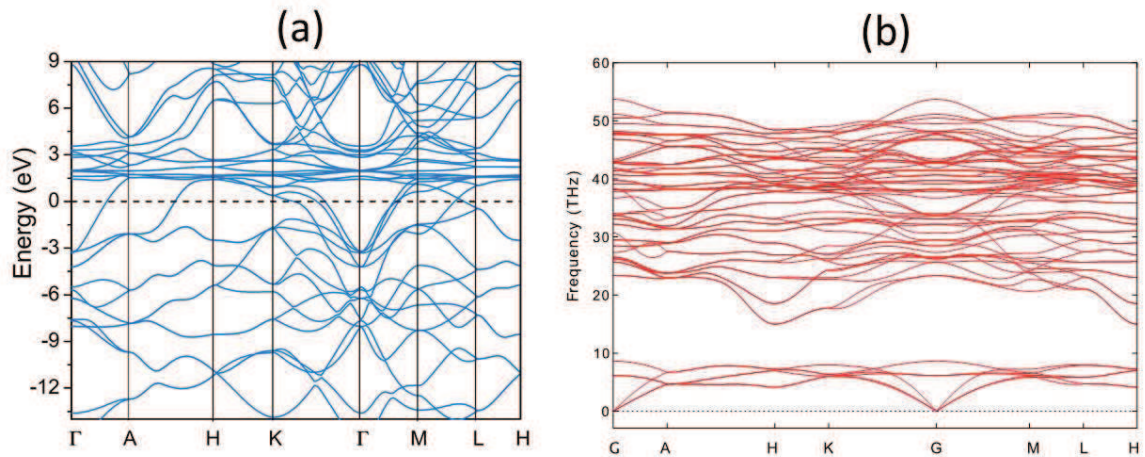


Figure 5: Electronic band structure and phonon dispersion curves for $P6_3/mmc$ -CeH₉ at 150 GPa in (a) and (b) respectively. Dotted line in (a) indicates Fermi level. Absence of imaginary phonons in the dispersion curves Fig. (b) shows the dynamical stability of $P6_3/mmc$ -CeH₉ at 150 GPa. Phonon instability at 120 GPa is shown in supplementary Fig. S10.

In summary, we have successfully synthesized a cerium superhydride phase of CeH₉ below 100 GPa crystallizing in the hexagonal $P6_3/mmc$ clathrate structure. In addition to this we have also synthesized a new cubic phase of CeH₃ with space group $Pm\bar{3}n$ (β -UH₃ type), which was recovered at ambient phase after complete decompression. Our studies give strong evidence for the synthesis of rare earth superhydrides and pave the way for future studies on other rare earth-hydrogen systems under extreme pressure with the aid of laser heating perhaps to make the binary hydrides MH_x with $x > 9$. Apart from this, the estimated T_c of 117 K in $P6_3/mmc$ -CeH₉ at 200 GPa is very promising. Electron-phonon coupling in $P6_3/mmc$ -CeH₉ is even higher than in H₃S but still could not achieve higher T_c due to lower logarithmic average phonon frequency. Conspicuously, the dense 3-dimensional atomic hydrogen sublattice is noted for superhydride $P6_3/mmc$ -CeH₉ as compared with reported super/poly-hydrides and similar to atomic metallic hydrogen at 100 GPa. The discovery of CeH₉ at a feasible pressure range with prediction of superconductivity will certainly inspire further studies to gain in-depth understanding of hydrogen interaction in atomic hydrogen and conventional superconductivity.

Methods

Experimental Details. High pressure-temperature (P - T) experiments were carried out using a single-sided laser heated DAC with a pair of bevelled diamond anvils of size 100-300 μm culets. Polycrystalline cerium (*Alfa Aesar*, 99.9 % purity) sample of ~ 5 μm thickness was loaded inside a sample chamber drilled to a diameter of 75 μm in a rhenium gasket of 250 μm initial thickness pre-indented to 18 μm . Cerium is very likely to oxidize in open air so the sample was loaded in an argon filled glove box where both H₂O and O₂ concentrations were maintained below 0.1 ppm. A small piece of gold (~ 5 μm width) was also placed near the sample for pressure calibration as shown in supplementary Fig. S14. For hydrogen loading, sample chamber was initially sealed by slightly closing the gasket and then opened in the high-pressure gas loading system in order to fill it with high purity hydrogen gas at room temperature under ~ 1.7 kilo-bar pressure. After hydrogen loading, Raman spectra of the H₂ vibron, collected at 9 GPa from the sample chamber, confirmed the presence of H₂ inside the sample chamber (supplementary Fig. S15). XRD patterns were recorded at beamline 13-IDD of GSECARS at the Advanced Photon Source. Angle-dispersive XRD patterns were recorded on a PILATUS CdTe 1M detector with a synchrotron radiation of incident wavelength 0.3344 \AA

focused to a spot size of $\sim 3 \times 4 \mu\text{m}$ (FWHM). A clean-up slit with an $8 \mu\text{m}$ size pin-hole was used to cut down the beam tails and collect the XRD from the smallest area possible. Pulsed laser-heating was carried out using the online infrared laser set-up with a wavelength of 1064 nm available at beamline 13-IDD⁵³. Several cycles of laser heating were carried at each pressure of 33, 60, 80, 89, 98 and 100 GPa during compression and at 79 and 54 GPa during the decompression run. The use of the pulse laser heating not just helped to promote reaction between Ce and H_2 to form cerium hydrides but also reduced the possibility of diamond anvil failure. Pulsed-laser heating with microsecond pulse width has been utilized to reach temperatures of $1,000\text{-}2,000 \text{ K}$. Every laser heating shot was formed by accumulating 300k frequency modulated laser pulses of one microsecond pulse-width at a rate of 10kHz . The flat top of the laser heating spot size was around $10 \mu\text{m}$ in diameter. We strictly avoided temperatures above 2000 K to protect diamonds as hydrogen loaded DACs at high P - T conditions are most likely to fail^{32,54}. Maintaining the sample temperature below 2000 K and relatively cold surrounding area using pulsed heating mode helped to avoid contamination and parasitic reaction with the sample chamber wall of gasket. Also, the laser heating spot on the sample was consistently maintained at substantial distance from gasket wall to avoid any contamination due to unwanted reaction (see supplementary Fig. S16). *In situ* temperature measurements were carried by fitting the slope of thermal radiation spectra to a Planck radiation function. Uncertainty in temperature measurements were less than $\pm 100 \text{ K}$. Obtained raw images of XRD were integrated with DIOPTAS software⁵⁵. Rietveld and Le Bail refinements were carried out using FullPROF software.

Calculation Details. Evolutionary variable-composition simulation, implemented in USPEX, is used to explore the high-pressure phase diagram of the Ce-H system from ambient pressure to 250 GPa . The evolutionary algorithm USPEX⁵⁶⁻⁶⁰ is a powerful method for finding thermodynamically stable compounds of a given system and their most stable structures. This method has been shown to be successful in predicting high-pressure structures of variety of systems which were confirmed experimentally, in specific superconducting hydrides, e.g., UH_8 ³⁰ and H_3S ¹⁴. In this method, the first generation of structures (100 structures) and compositions are created using the random symmetric algorithm. Subsequent generations were obtained using 40% heredity, 20% transmutation, 20% softmutation, and 20% random symmetric generator. We allowed variation operators to automatically evolve in the subsequent generations. The underlying structure relaxations were carried out using the VASP package⁶⁰ in the framework of DFT and using PBE-GGA (Perdew-Burke-Ernzerhof generalized gradient

approximation)^{61,62}. We believe PBE is the most appropriate choice, because PBE best reproduces the experimental data (see supplementary Fig. S17 and Tables S4 and S5). The projector-augmented wave approach (PAW)^{60,63} was used to describe the core electrons and their effects on valence orbitals. Valence electron configuration of $5s^25p^64f^15d^16s^2$ (i.e., with explicitly included f electrons) and $1s^1$ was used for the Ce and H atoms, respectively. A plane-wave kinetic-energy cut off of 1000 eV for hard PAW potentials and dense Monkhorst-Pack k-points grids with reciprocal space resolution of $2\pi \times 0.03 \text{ \AA}^{-1}$ were employed⁶⁴ to sample the Brillouin zone. Phonon frequencies and superconducting critical temperature were calculated using density-functional perturbation theory as implemented in the QUANTUM ESPRESSO package⁶⁵, also using the PBE-GGA functional. Ultrasoft pseudopotentials for Ce and H were used with a plane-wave basis set cut-off of 70 Ry, which gives a convergence in energy with a precision of 1 meV/atom. Phonon dispersions were also calculated under the quasi-harmonic approximation using the finite displacement method implemented in PHONOPY package⁶⁶ using forces computed with VASP. The k-space integration (electrons) was approximated by a summation over a $12 \times 12 \times 6$ uniform grid in reciprocal space, with the smearing scheme of Methfessel-Paxton and a fictitious smearing temperature T of $k_B T = 0.05$ Ry for self-consistent cycles and relaxations; a much finer ($24 \times 24 \times 12$) grid was used for evaluating DOS and electron-phonon linewidths. Dynamical matrices and electron-phonon linewidths of $P6_3/mmc$ -CeH₉ were calculated on a uniform $6 \times 6 \times 3$ grid in q-space. The superconducting transition temperature T_c was estimated using the Allen-Dynes modified McMillan equation⁶⁷

$$T_c = \frac{\omega_{\log}}{1.2} \exp\left(\frac{-1.04(1+\lambda)}{\lambda - \mu^*(1+0.62\lambda)}\right), \quad (1)$$

where μ^* is the Coulomb pseudopotential and ω_{\log} is the logarithmic average phonon frequency. The electron-phonon coupling constant λ and ω_{\log} were calculated as

$$\omega_{\log} = \exp\left(\frac{2}{\lambda} \int \frac{d\omega}{\omega} \alpha^2 F(\omega) \ln(\omega)\right), \quad (2)$$

$$\lambda = 2 \int_0^\infty \frac{\alpha^2 F(\omega)}{\omega} d\omega \quad (3)$$

Acknowledgements

The authors thank Suyu Fu of UT Austin for his assistance for the XRD data collection and Yuyong Xiong for hydrogen loading at Center for High Pressure Science and Technology

Advanced Research (HPSTAR). J.Z., A.O., and J.F.L acknowledge the support from DOD-ARMY grant (W911NF-16-1-0559). M.M.D.E acknowledges support from the National Science Foundation (EAR-1723160) for supporting this work. J.F.L acknowledges support from the National Science Foundation of China (NSFC) (Grant No. 11872077). N.P.S., Y.Z. and J.F.L. acknowledges support from HPSTAR. Y.Z. acknowledges support from “the Fundamental Research Funds for the central universities” in China and from the NSFC (Grant No. 41804082). High-pressure XRD experiments were conducted at GeoSoilEnviroCARS of APS, ANL. GeoSoilEnviroCARS operations are supported by the National Science Foundation-Earth Sciences (EAR-1128799) and the Department of Energy, Geosciences (DE-FG02-94ER14466). This research used resources of the Advanced Photon Source, a U.S. Department of Energy (DOE) Office of Science User Facility operated for the DOE Office of Science by Argonne National Laboratory under Contract No. DE-AC02-06CH11357. Calculations were mainly performed on the cluster (QSH) in our laboratory at Stony Brook University.

Author contributions

J.F.L. and N.P.S. conceived the project. J.F.L. supervised the project, and J.F.L. and N.P.S. coordinated the project. N.P.S. planned the experiment and prepared the diamond anvil cell samples. Y.Z., J.F.L., E.G. and V.B.P. carried out the XRD measurements with the laser heating at high pressures. N.P.S. analysed and modelled the data, N.P.S. and J.F.L. interpreted the initial data. M.M.D.E., I.A.K. and A.R.O. carried out the theoretical calculations. All the authors discussed the results. N.P.S. and M. M. D. E. wrote the draft. A.R.O., and J.F.L. participated in writing and revising the manuscript, and J.Z. and J.F.L. helped with the draft abstract. All the authors read and commented on the manuscript.

References

- 1 Wigner, E. & Huntington, H. B. On the Possibility of a Metallic Modification of Hydrogen. *The Journal of Chemical Physics* **3**, 764-770, doi:10.1063/1.1749590 (1935).
- 2 Ashcroft, N. W. Metallic Hydrogen: A High-Temperature Superconductor? *Physical Review Letters* **21**, 1748-1749 (1968).
- 3 Loubeyre, P., Occelli, F. & LeToullec, R. Optical studies of solid hydrogen to 320 GPa and evidence for black hydrogen. *Nature* **416**, 613, doi:10.1038/416613a (2002).
- 4 Eremets, M. I. & Troyan, I. A. Conductive dense hydrogen. *Nature Materials* **10**, 927, doi:10.1038/nmat3175 (2011).
- 5 Dalladay-Simpson, P., Howie, R. T. & Gregoryanz, E. Evidence for a new phase of dense hydrogen above 325 gigapascals. *Nature* **529**, 63, doi:10.1038/nature16164 (2016).

- 6 Dias, R. P. & Silvera, I. F. Observation of the Wigner-Huntington transition to metallic hydrogen. *Science* (2017).
- 7 Borinaga, M., Errea, I., Calandra, M., Mauri, F. & Bergara, A. Anharmonic effects in atomic hydrogen: Superconductivity and lattice dynamical stability. *Physical Review B* **93**, 174308 (2016).
- 8 Azadi, S., Monserrat, B., Foulkes, W. M. C. & Needs, R. J. Dissociation of High-Pressure Solid Molecular Hydrogen: A Quantum Monte Carlo and Anharmonic Vibrational Study. *Physical Review Letters* **112**, 165501 (2014).
- 9 McMinis, J., Clay, R. C., Lee, D. & Morales, M. A. Molecular to Atomic Phase Transition in Hydrogen under High Pressure. *Physical Review Letters* **114**, 105305 (2015).
- 10 Gor'kov, L. P. & Kresin, V. Z. Colloquium: High pressure and road to room temperature superconductivity. *Reviews of Modern Physics* **90**, 011001 (2018).
- 11 Ashcroft, N. W. Hydrogen Dominant Metallic Alloys: High Temperature Superconductors? *Physical Review Letters* **92**, 187002 (2004).
- 12 Struzhkin, V. V. Superconductivity in compressed hydrogen-rich materials: Pressing on hydrogen. *Physica C: Superconductivity and its Applications* **514**, 77-85, doi:<https://doi.org/10.1016/j.physc.2015.02.017> (2015).
- 13 McMahan, J. M. & Ceperley, D. M. High-temperature superconductivity in atomic metallic hydrogen. *Physical Review B* **84**, 144515 (2011).
- 14 Duan, D. *et al.* Pressure-induced metallization of dense (H₂S)₂H₂ with high-T_c superconductivity. *Scientific Reports* **4**, 6968, doi:10.1038/srep06968 (2014).
- 15 Drozdov, A. P., Erements, M. I., Troyan, I. A., Ksenofontov, V. & Shylin, S. I. Conventional superconductivity at 203 kelvin at high pressures in the sulfur hydride system. *Nature* **525**, 73, doi:10.1038/nature14964 (2015).
- 16 Shaw, B. L. in *Inorganic Hydrides* 1-3 (Pergamon, 1967).
- 17 Blackledge, J. P. in *Metal Hydrides* 1-20 (Academic Press, 1968).
- 18 Zurek, E. Hydrides of the Alkali Metals and Alkaline Earth Metals Under Pressure. *Comments on Inorganic Chemistry* **37**, 78-98, doi:10.1080/02603594.2016.1196679 (2017).
- 19 Zeng, Q., Yu, S., Li, D., Oganov, A. R. & Frapper, G. Emergence of novel hydrogen chlorides under high pressure. *Physical Chemistry Chemical Physics* **19**, 8236-8242, doi:10.1039/C6CP08708F (2017).
- 20 Mahdi Davari Esfahani, M. *et al.* Superconductivity of novel tin hydrides (SnnHm) under pressure. *Scientific Reports* **6**, 22873, doi:10.1038/srep22873 (2016).
- 21 Peng, F. *et al.* Hydrogen Clathrate Structures in Rare Earth Hydrides at High Pressures: Possible Route to Room-Temperature Superconductivity. *Physical Review Letters* **119**, 107001 (2017).
- 22 Wang, H., Tse, J. S., Tanaka, K., Iitaka, T. & Ma, Y. Superconductive sodalite-like clathrate calcium hydride at high pressures. *Proceedings of the National Academy of Sciences* **109**, 6463-6466, doi:10.1073/pnas.1118168109 (2012).
- 23 Lonie, D. C., Hooper, J., Altintas, B. & Zurek, E. Metallization of magnesium polyhydrides under pressure. *Physical Review B* **87**, 054107 (2013).
- 24 Feng, X., Zhang, J., Gao, G., Liu, H. & Wang, H. Compressed sodalite-like MgH₆ as a potential high-temperature superconductor. *RSC Advances* **5**, 59292-59296, doi:10.1039/C5RA11459D (2015).
- 25 Li, Y. *et al.* Pressure-stabilized superconductive yttrium hydrides. *Scientific Reports* **5**, 9948, doi:10.1038/srep09948 (2015).
- 26 Liu, H., Naumov, I. I., Hoffmann, R., Ashcroft, N. W. & Hemley, R. J. Potential high T_c superconducting lanthanum and yttrium hydrides at high pressure. *Proceedings of the National Academy of Sciences* **114**, 6990-6995, doi:10.1073/pnas.1704505114 (2017).
- 27 Semenok, D. V., Kvashnin, A. G., Kruglov, I. A. & Oganov, A. R. Actinium Hydrides AcH₁₀, AcH₁₂, and AcH₁₆ as High-Temperature Conventional Superconductors. *The Journal of Physical Chemistry Letters*, 1920-1926, doi:10.1021/acs.jpcclett.8b00615 (2018).

- 28 Pépin, C. M., Geneste, G., Dewaele, A., Mezouar, M. & Loubeyre, P. Synthesis of FeH₅: A layered structure with atomic hydrogen slabs. *Science* **357**, 382-385, doi:10.1126/science.aan0961 (2017).
- 29 Geballe, Z. M. *et al.* Synthesis and Stability of Lanthanum Superhydrides. *Angewandte Chemie International Edition* **57**, 688-692, doi:10.1002/anie.201709970 (2018).
- 30 Kruglov, I. A. *et al.* Uranium polyhydrides at moderate pressures: prediction, synthesis, and expected superconductivity. *arXiv:1708.05251* (2017).
- 31 Pépin, C., Loubeyre, P., Occelli, F. & Dumas, P. Synthesis of lithium polyhydrides above 130 GPa at 300 K. *Proceedings of the National Academy of Sciences* **112**, 7673-7676, doi:10.1073/pnas.1507508112 (2015).
- 32 Struzhkin, V. V. *et al.* Synthesis of sodium polyhydrides at high pressures. *Nature Communications* **7**, 12267, doi:10.1038/ncomms12267 (2016).
- 33 Somayazulu, M. *et al.* Pressure-induced bonding and compound formation in xenon–hydrogen solids. *Nature Chemistry* **2**, 50, doi:10.1038/nchem.445 (2009).
- 34 Binns, J. *et al.* Formation of H_2 -rich iodine-hydrogen compounds at high pressure. *Physical Review B* **97**, 024111 (2018).
- 35 Somayazulu, M. *et al.* Evidence for superconductivity above 260 K in lanthanum superhydride at megabar pressures. *arXiv arXiv:1808.07695* (2018).
- 36 Drozdov, A. P. *et al.* Superconductivity at 215 K in lanthanum hydride at high pressures. *arXiv arXiv:1808.07039* (2018).
- 37 Crabtree, G. W., Dresselhaus, M. S. & Buchanan, M. V. The Hydrogen Economy. *Physics Today* **57**, 39-44, doi:10.1063/1.1878333 (2004).
- 38 Halevy, I., Salhov, S., Zalkind, S., Brill, M. & Yaar, I. High pressure study of β -UH₃ crystallographic and electronic structure. *Journal of Alloys and Compounds* **370**, 59-64, doi:<https://doi.org/10.1016/j.jallcom.2003.09.124> (2004).
- 39 Ce, M. *et al.* Structure phase transformation and equation of state of cerium metal under pressures up to 51 GPa. *Chinese Physics B* **25**, 046401 (2016).
- 40 Lipp, M. J. *et al.* Comparison of the high-pressure behavior of the cerium oxides Ce_2O_3 and CeO_2 . *Physical Review B* **93**, 064106 (2016).
- 41 Jacobsen, M. K., Velisavljevic, N., Dattelbaum, D. M., Chellappa, R. S. & Park, C. High pressure and temperature equation of state and spectroscopic study of CeO₂. *Journal of Physics: Condensed Matter* **28**, 155401 (2016).
- 42 Davari Esfahani, M. M., Oganov, A. R., Niu, H. & Zhang, J. Superconductivity and unexpected chemistry of germanium hydrides under pressure. *Physical Review B* **95**, 134506, doi:10.1103/PhysRevB.95.134506 (2017).
- 43 Loubeyre, P. *et al.* X-ray diffraction and equation of state of hydrogen at megabar pressures. *Nature* **383**, 702, doi:10.1038/383702a0 (1996).
- 44 Pépin, C. M., Dewaele, A., Geneste, G., Loubeyre, P. & Mezouar, M. New Iron Hydrides under High Pressure. *Physical Review Letters* **113**, 265504 (2014).
- 45 Goncharenko, I. *et al.* Pressure-Induced Hydrogen-Dominant Metallic State in Aluminum Hydride. *Physical Review Letters* **100**, 045504 (2008).
- 46 McMahan, J. M. & Ceperley, D. M. Ground-State Structures of Atomic Metallic Hydrogen. *Physical Review Letters* **106**, 165302 (2011).
- 47 Tanaka, K., Tse, J. S. & Liu, H. Electron-phonon coupling mechanisms for hydrogen-rich metals at high pressure. *Physical Review B* **96**, 100502, doi:10.1103/PhysRevB.96.100502 (2017).
- 48 Vohra, Y. K., Beaver, S. L., Akella, J., Ruddle, C. A. & Weir, S. T. Ultrapressure equation of state of cerium metal to 208 GPa. *Journal of Applied Physics* **85**, 2451-2453, doi:10.1063/1.369566 (1999).

- 49 Carbotte, J. P., Nicol, E. J. & Timusk, T. Detecting Superconductivity in the High Pressure Hydrides and Metallic Hydrogen from Optical Properties. *Physical Review Letters* **121**, 047002, doi:10.1103/PhysRevLett.121.047002 (2018).
- 50 Zhu, Q., Oganov, A. R., Lyakhov, A. O. & Yu, X. Generalized evolutionary metadynamics for sampling the energy landscapes and its applications. *Physical Review B* **92**, 024106 (2015).
- 51 Errea, I. *et al.* High-Pressure Hydrogen Sulfide from First Principles: A Strongly Anharmonic Phonon-Mediated Superconductor. *Physical Review Letters* **114**, 157004, doi:10.1103/PhysRevLett.114.157004 (2015).
- 52 Errea, I. *et al.* Quantum hydrogen-bond symmetrization in the superconducting hydrogen sulfide system. *Nature* **532**, 81, doi:10.1038/nature17175 (2016).
- 53 Prakapenka, V. B. *et al.* Advanced flat top laser heating system for high pressure research at GSECARS: application to the melting behavior of germanium. *High Pressure Research* **28**, 225-235, doi:10.1080/08957950802050718 (2008).
- 54 Goncharov, A. F. *et al.* X-ray diffraction in the pulsed laser heated diamond anvil cell. *Review of Scientific Instruments* **81**, 113902, doi:10.1063/1.3499358 (2010).
- 55 Prescher, C. & Prakapenka, V. B. DIOPTAS: a program for reduction of two-dimensional X-ray diffraction data and data exploration. *High Pressure Research* **35**, 223-230, doi:10.1080/08957959.2015.1059835 (2015).
- 56 Glass, C. W., Oganov, A. R. & Hansen, N. USPEX—Evolutionary crystal structure prediction. *Computer Physics Communications* **175**, 713-720, doi:<https://doi.org/10.1016/j.cpc.2006.07.020> (2006).
- 57 Oganov, A. R. & Glass, C. W. Crystal structure prediction using ab initio evolutionary techniques: Principles and applications. *The Journal of Chemical Physics* **124**, 244704, doi:10.1063/1.2210932 (2006).
- 58 Lyakhov, A. O., Oganov, A. R. & Valle, M. How to predict very large and complex crystal structures. *Computer Physics Communications* **181**, 1623-1632, doi:<https://doi.org/10.1016/j.cpc.2010.06.007> (2010).
- 59 Oganov, A. R., Lyakhov, A. O. & Valle, M. How Evolutionary Crystal Structure Prediction Works—and Why. *Accounts of Chemical Research* **44**, 227-237, doi:10.1021/ar1001318 (2011).
- 60 Kresse, G. & Joubert, D. From ultrasoft pseudopotentials to the projector augmented-wave method. *Physical Review B* **59**, 1758-1775 (1999).
- 61 Perdew, J. P., Burke, K. & Ernzerhof, M. Generalized Gradient Approximation Made Simple. *Physical Review Letters* **77**, 3865-3868 (1996).
- 62 Perdew, J. P., Burke, K. & Ernzerhof, M. Generalized Gradient Approximation Made Simple [Phys. Rev. Lett. 77, 3865 (1996)]. *Physical Review Letters* **78**, 1396-1396 (1997).
- 63 Blöchl, P. E. Projector augmented-wave method. *Physical Review B* **50**, 17953-17979 (1994).
- 64 Monkhorst, H. J. & Pack, J. D. Special points for Brillouin-zone integrations. *Physical Review B* **13**, 5188-5192 (1976).
- 65 Paolo, G. *et al.* QUANTUM ESPRESSO: a modular and open-source software project for quantum simulations of materials. *Journal of Physics: Condensed Matter* **21**, 395502 (2009).
- 66 Togo, A. & Tanaka, I. First principles phonon calculations in materials science. *Scripta Materialia* **108**, 1-5, doi:<https://doi.org/10.1016/j.scriptamat.2015.07.021> (2015).
- 67 Allen, P. B. & Dynes, R. C. Transition temperature of strong-coupled superconductors reanalyzed. *Physical Review B* **12**, 905-922 (1975).

Supplementary Information for

Synthesis of clathrate cerium superhydride CeH₉ below 100 GPa with atomic hydrogen sublattice

Nilesh P. Salke¹, M. Mahdi Davari Esfahani², Youjun Zhang^{3,1}, Ivan A. Kruglov^{4,5}, Jianshi Zhou⁶,
Yaguo Wang⁶, Eran Greenberg⁷, Vitali B. Prakapenka⁷, Artem R. Oganov^{8,4,9,*}, Jung-Fu Lin^{10,*}

¹Center for High Pressure Science & Technology Advanced Research (HPSTAR), Shanghai, 201203, China

²Department of Geosciences, Center for Materials by Design, and Institute for Advanced Computational
Science, State University of New York, Stony Brook, New York 11794-2100, USA

³Institute of Atomic and Molecular Physics, Sichuan University, Chengdu 610065, China

⁴Department of Problems of Physics and Energetics, Moscow Institute of Physics and Technology, 9 Institutskiy
Lane, Dolgoprudny City, Moscow Region 141700, Russia

⁵Dukhov Research Institute of Automatics (VNIIA), Moscow 127055, Russia

⁶Department of Mechanical Engineering, The University of Texas at Austin, Austin, Texas 78712, USA

⁷Center for Advanced Radiation Sources, University of Chicago, Illinois, 60637, USA

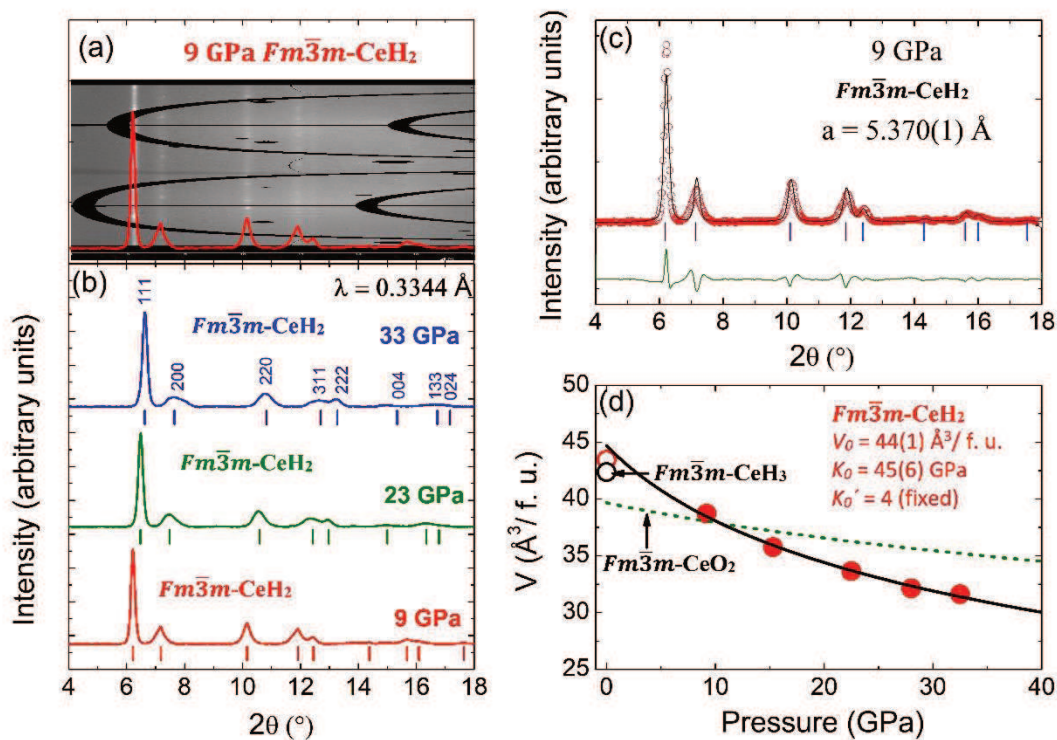
⁸Skolkovo Institute of Science and Technology, Skolkovo Innovation Center, 3 Nobel Street, Moscow 143026,
Russia

⁹International Center for Materials Design, Northwestern Polytechnical University, Xi'an 710072, China

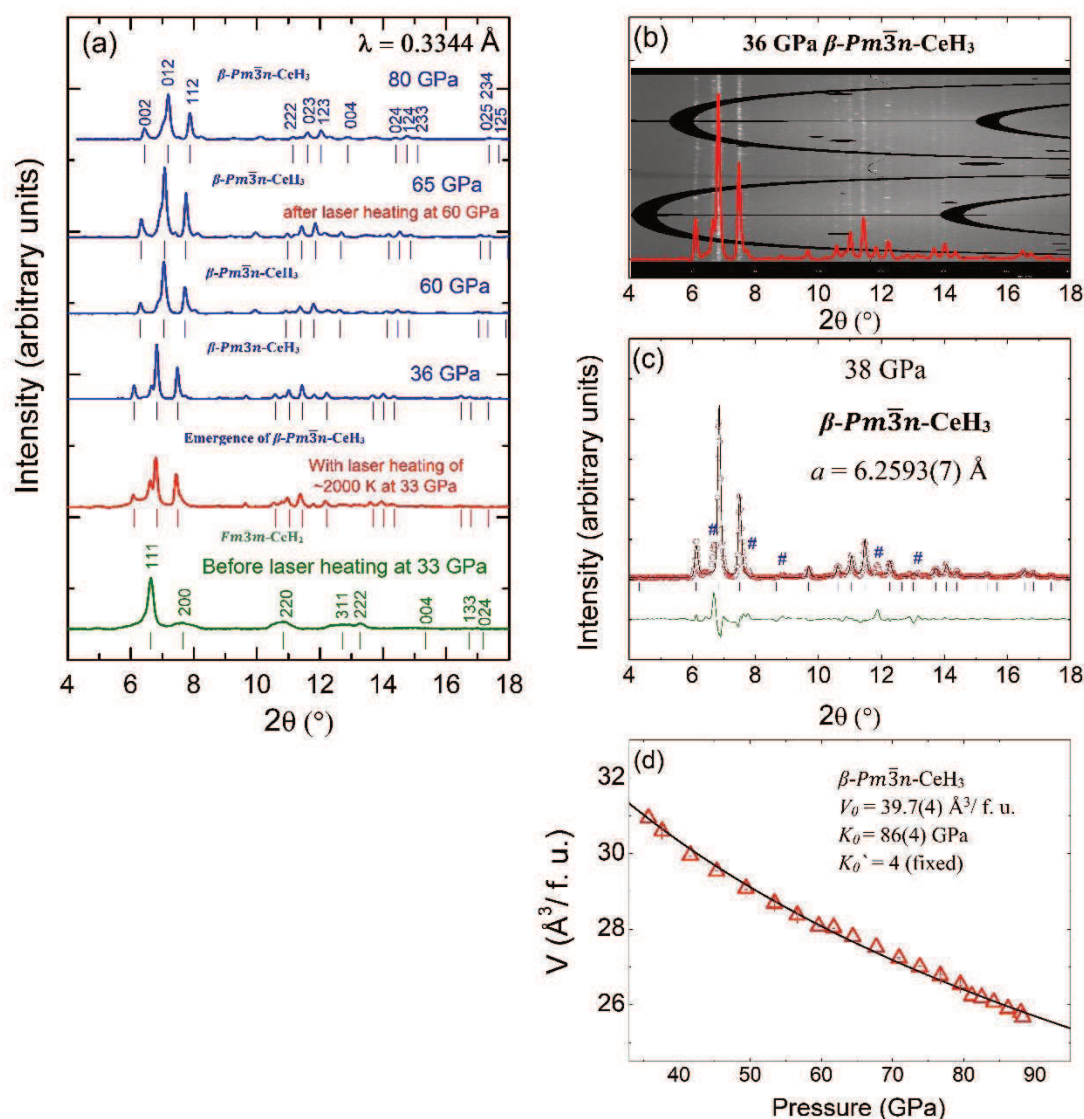
¹⁰Department of Geological Sciences, The University of Texas at Austin, Austin, Texas 78712, USA

XRD pattern of the sample initially loaded at 9 GPa could be indexed with $Fm\bar{3}m$ structure. From the literature, it is well known that at ambient P - T conditions CeH_X system can stabilize in various stoichiometries ranging from X = 2 to 3¹. Specifically, two extreme compositions CeH₂ and CeH₃ stabilize in $Fm\bar{3}m$ structure whereas CeH_{2.5} (Ce₂H₅) forms tetragonal structure with $I4_1md$ space group¹. Besides this, CeO₂, which could occur due to starting sample being contaminated and oxidized, also has fluorite type $Fm\bar{3}m$ structure². It was difficult to confirm the exact stoichiometry and composition of observed $Fm\bar{3}m$ phase at 9 GPa. It was also important to confirm stoichiometry and composition of the sample to rule out any contamination. Reported values of lattice parameter at ambient pressure for $Fm\bar{3}m$ structured CeH₂ and CeH₃ were 5.580 and 5.534 Å respectively³; corresponding volume per formula unit (V/f.u.) is 43.435 and 42.37 Å³ respectively³. We fitted the experimental V/f.u. (assuming Z=4) of observed $Fm\bar{3}m$ phase using third order Birch-Murnaghan EOS (see SI Figure S1d). Zero pressure volume obtained after fitting is $V_0 = 44(1)$ Å³/f.u., which is closer to the reported V_0 /f.u. of CeH₂, which rules out the $Fm\bar{3}m$ -CeH₃ phase. In Fig. S1d, we also compared the experimental EOS with reported EOS of CeO₂². From Fig. S1d, it clearly indicates that

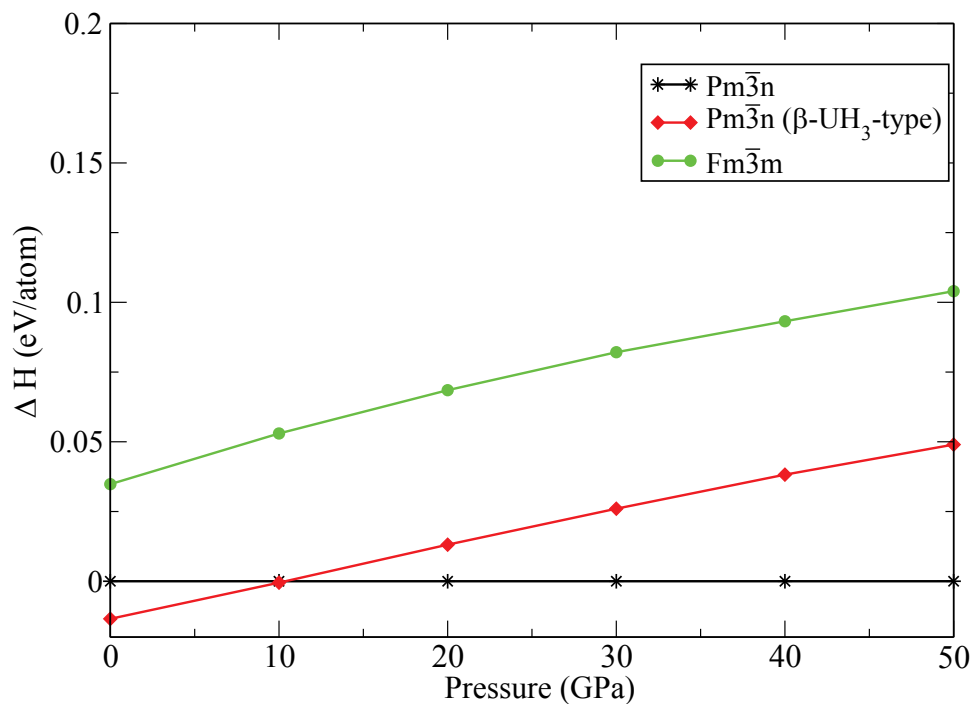
experimental EOS of $Fm\bar{3}m$ phase is not consistent with EOS of $Fm\bar{3}m$ -CeO₂ which firmly rules out the presence of $Fm\bar{3}m$ -CeO₂ in the sample. Hence, we concluded that $Fm\bar{3}m$ structure observed in the beginning at 9 GPa was of CeH₂ phase which persisted up to 33 GPa until we carried laser heating on the sample.



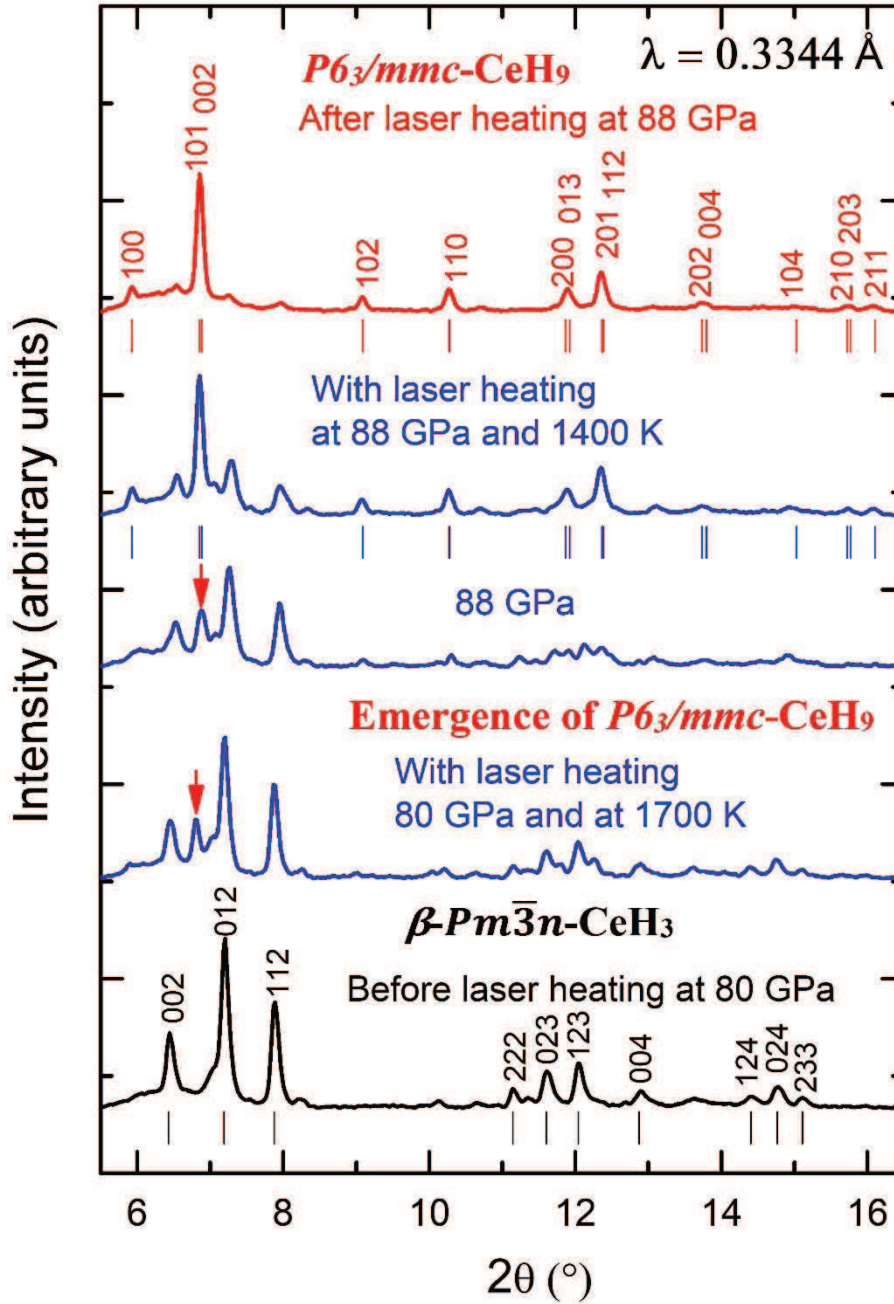
Supplementary Figure S1: Representative x-ray diffraction patterns at high pressures and equation of state of $Fm\bar{3}m$ -CeH₂. (a) XRD image at 9 GPa representing polycrystalline nature of $Fm\bar{3}m$ -CeH₂ phase. (b) X-ray diffraction patterns of $Fm\bar{3}m$ -CeH₂ from 9 to 33 GPa. Red, green and blue vertical ticks correspond to peak positions of $Fm\bar{3}m$ -CeH₂ phase at 9, 23 and 33 GPa respectively. (c) Le Bail refinement plot for $Fm\bar{3}m$ -CeH₂ at 9 GPa, $\chi^2 = 5.41$ (d) Volume per formula unit of $Fm\bar{3}m$ -CeH₂ as a function of pressure is fitted using third-order Birch-Murnaghan equation of state (EOS). Red solid circles represent experimental unit cell volume per formula unit data. Black line is EOS fit to experimental data. Red and black open circle represents reported volume per formula unit of $Fm\bar{3}m$ structured CeH₂ and CeH₃ at ambient pressure respectively.³ Green dotted line represents reported EOS for $Fm\bar{3}m$ -CeO₂.²



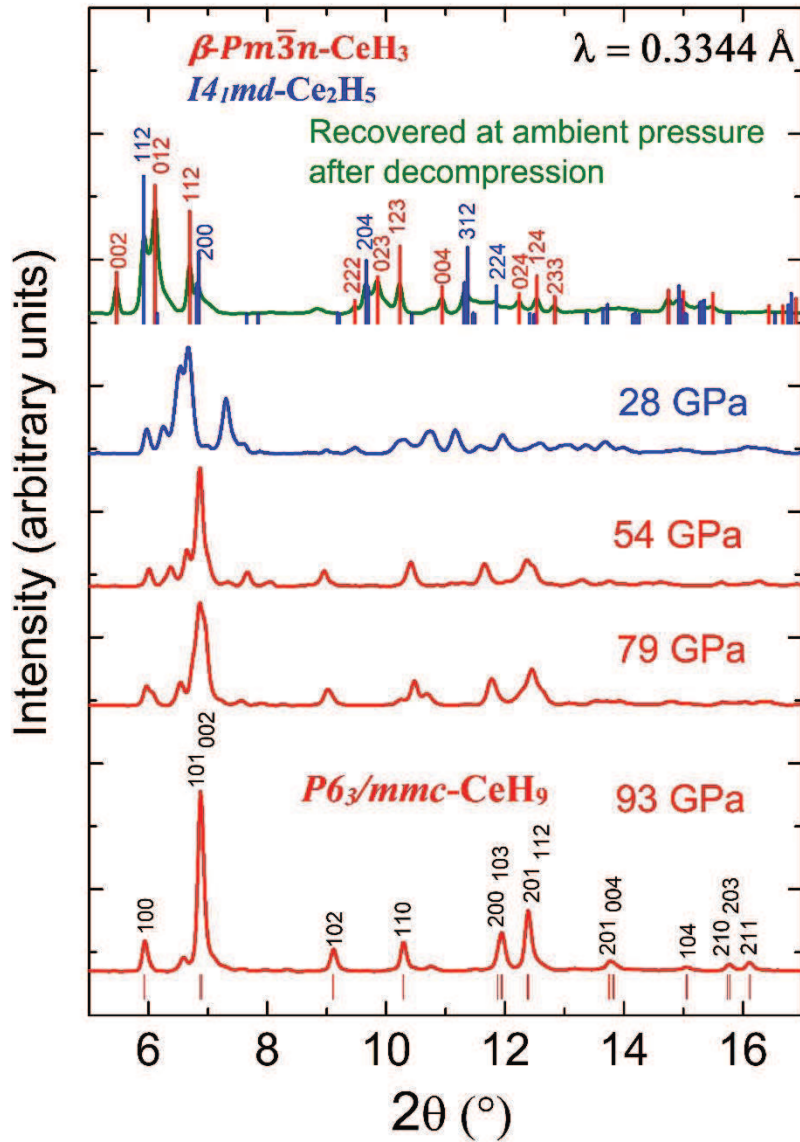
Supplementary Figure S2: Representative x-ray diffraction patterns denoting evolution of β - $Pm\bar{3}n$ - CeH_3 under pressure with laser heating and equation of state fitting. (a) X-ray diffraction patterns at various pressures representing the formation of β - $Pm\bar{3}n$ - CeH_3 up to 80 GPa. β - $Pm\bar{3}n$ - CeH_3 phase forms after laser heating at 33 GPa and 2100 K. Vertical green ticks indicate indexing of peak position for $Fm\bar{3}m$ - CeH_2 ; vertical red and blue ticks indicate indexing of peak position for β - $Pm\bar{3}n$ - CeH_3 at respective pressure. (b) XRD image at 36 GPa representing polycrystalline nature of β - $Pm\bar{3}n$ - CeH_3 . (c) Le Bail refinement plot for β - $Pm\bar{3}n$ - CeH_3 at 38 GPa, $\chi^2 = 10.6$, # represents unidentified peaks (d) Third-order Birch-Murnaghan equation of state fitting for β - $Pm\bar{3}n$ - CeH_3 . Red open triangles represent experimental data for β - $Pm\bar{3}n$ - CeH_3 , black solid line represent EOS fit. Errors are also plotted in (d) but are mostly too small to be seen.



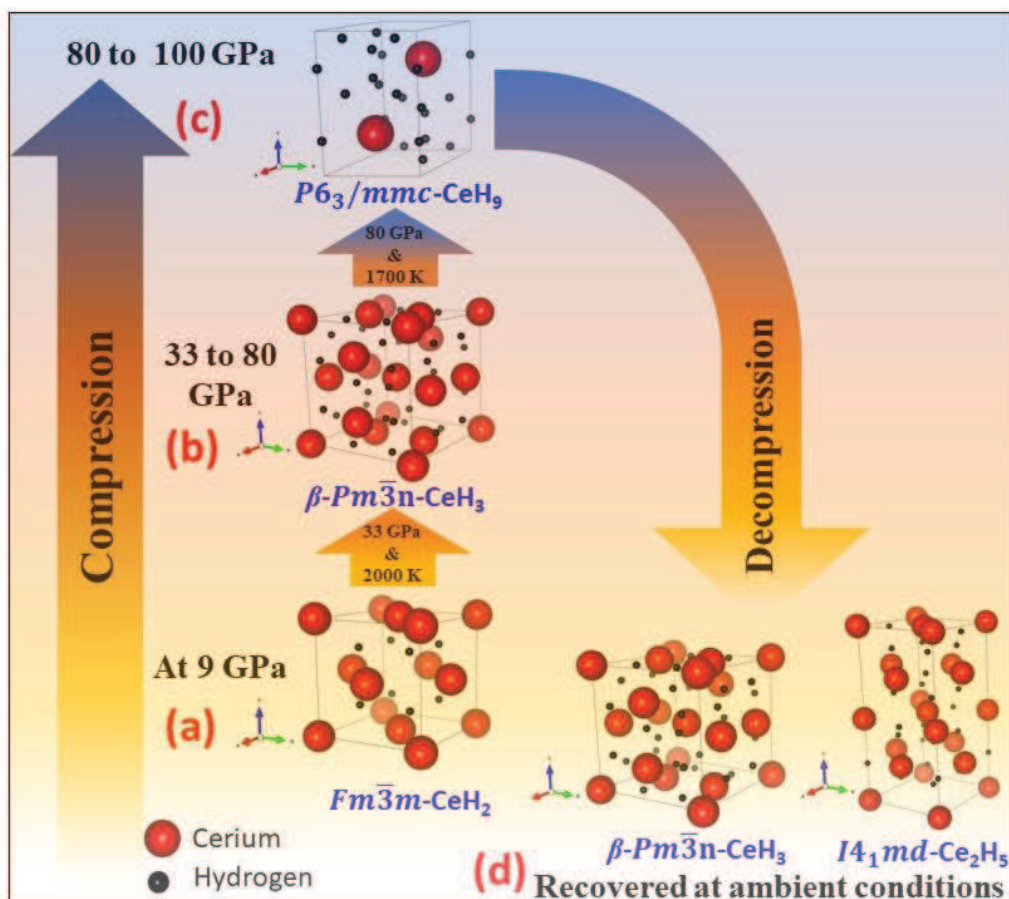
Supplementary Figure S3: Enthalpy comparison for various CeH_3 phases as a function of pressure. Enthalpy per atom relative to the $Pm\bar{3}n$ structure as a function of pressure for the best phases with the CeH_3 stoichiometry. Experimentally known ambient pressure phase $Fm\bar{3}m$ - CeH_3 is added for comparison. Red, black and green symbols-line represents β - $Pm\bar{3}n$, $Pm\bar{3}n$ and $Fm\bar{3}m$ phases of CeH_3 respectively.



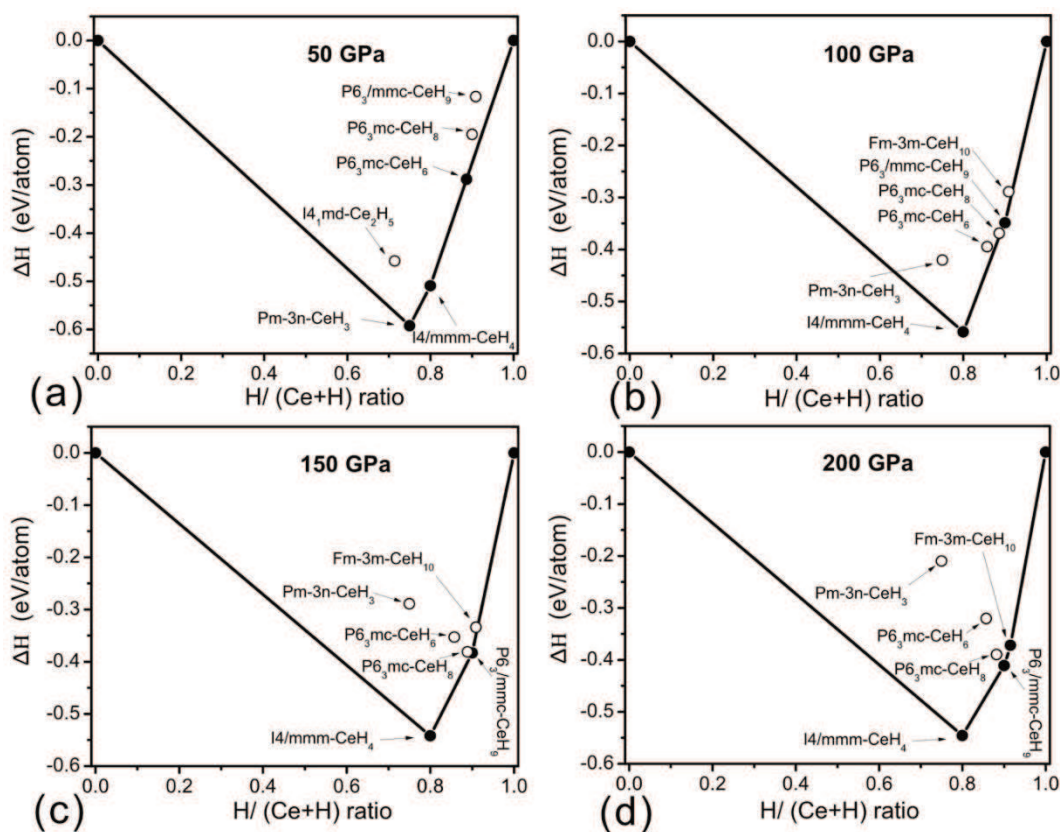
Supplementary Figure S4: X-ray diffraction patterns representing formation of superhydride $P6_3/mmc$ - CeH_9 . X-ray diffraction patterns at pressures above 80 GPa representing the formation of CeH_9 with laser heating. New peaks, which emerged after laser heating to 1700 K at 80 GPa, are shown with a red arrow corresponding to (101) and (002) of the $P6_3/mmc$ phase. Vertical black ticks indicate indexing for β - $Pm\bar{3}n$ - CeH_3 at 80 GPa. Vertical blue and red ticks indicate indexing of the $P6_3/mmc$ - CeH_9 phase at the respective pressures.



Supplementary Figure S5: Representative x-ray diffraction patterns obtained during the decompression cycle. XRD patterns were recorded upon the decompression cycle down to ambient pressure. Ambient pressure diffraction patterns of the recovered sample were recorded from the sample chamber after complete decompression. $Pm\bar{3}n$ -CeH₃ and $I4_1md$ -Ce₂H₅ phases were recovered at ambient conditions. Red vertical ticks for XRD at 93 GPa represent peak positions for $P6_3/mmc$ -CeH₉. Red and blue vertical lines for XRD of the recovered sample at ambient pressure indicate peak positions with relative intensity for $Pm\bar{3}n$ -CeH₃ and $I4_1md$ -Ce₂H₅, respectively.



Supplementary Figure S6: Pressure temperature path for the synthesis and stability of various Ce-H phases. (a) Starting at 9 GPa, cerium reacts with hydrogen to form $Fm\bar{3}m$ -CeH₂, which remained stable up to 33 GPa. (b) At 33 GPa with laser heating, $Fm\bar{3}m$ -CeH₂ in H₂ medium reacted to form β - $Pm\bar{3}n$ -CeH₃. β - $Pm\bar{3}n$ -CeH₃ remained stable up to 80 GPa (c) Laser heating of β - $Pm\bar{3}n$ -CeH₃ in H₂ medium above 80 GPa resulted in the discovery of the $P6_3/mmc$ -CeH₉ superhydride. The superhydride phase was found to be stable up to the maximum pressure reached in our studies i.e. 100 GPa. (d) After complete decompression, β - $Pm\bar{3}n$ -CeH₃ and $I4_1md$ -Ce₂H₅ were recovered at ambient conditions.



Supplementary Figure S7: Convex Hull diagram of Ce-H system. Predicted formation enthalpy of $Ce_{1-x}H_x$ as a function of H concentration at selected pressures. Open circles above the convex hull show unstable compounds with respect to decomposition into the two adjacent phases on the convex hull, while solid circles show thermodynamically stable compounds.

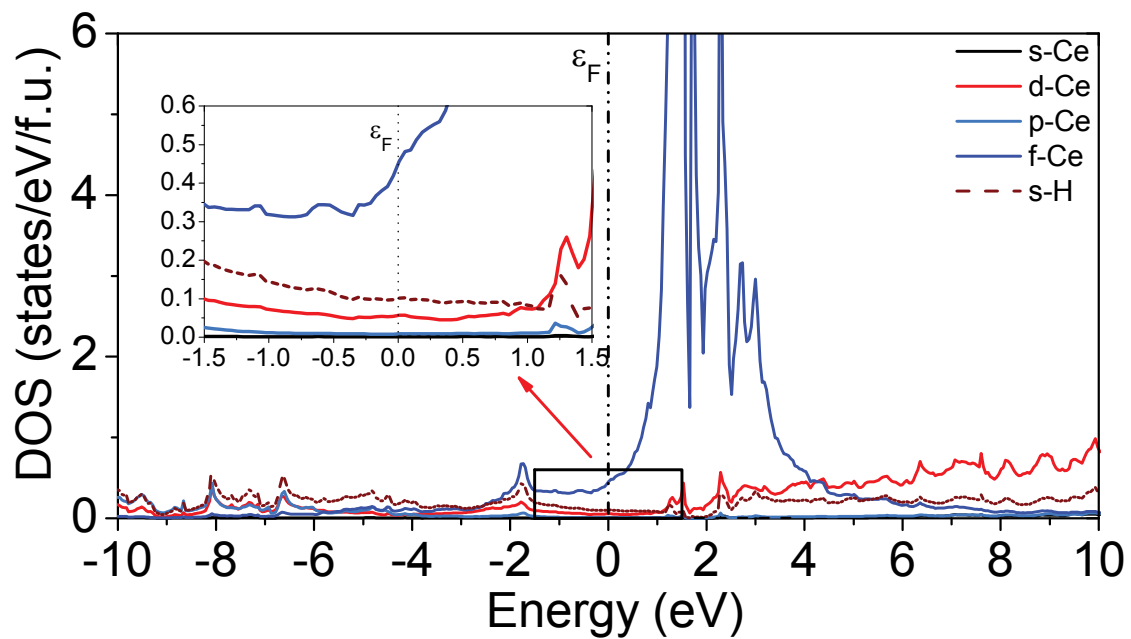


Figure S8: Electron density of states (DOS) for CeH₉ at 150 GPa. Electron DOS at Fermi level is largely dominated by Ce-4f and H orbitals.

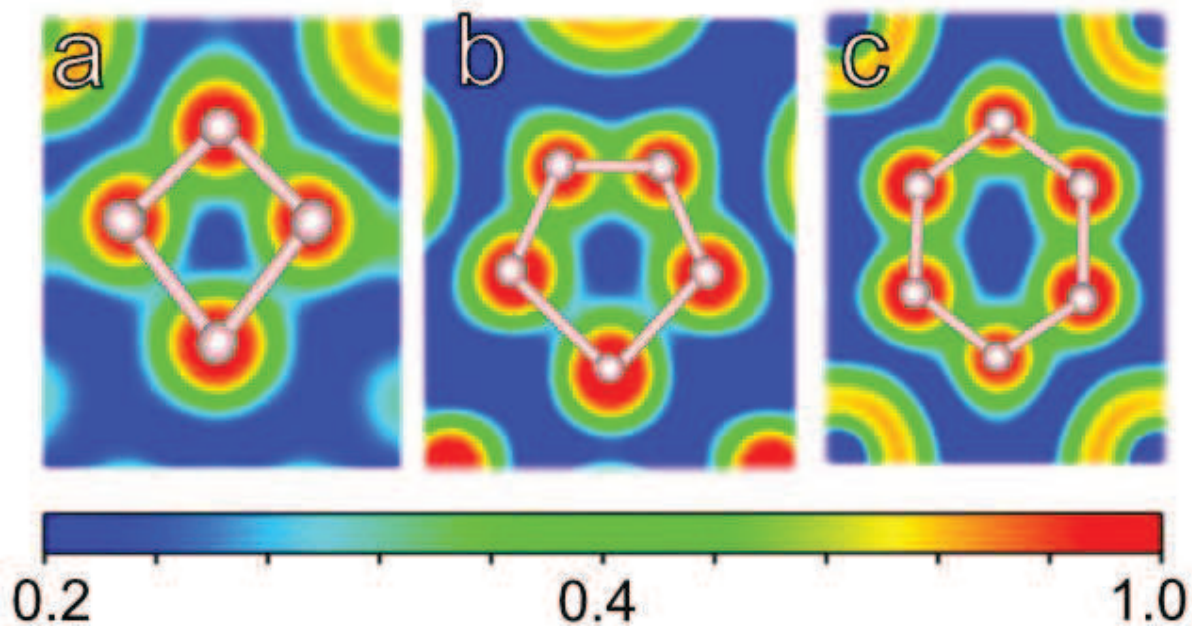
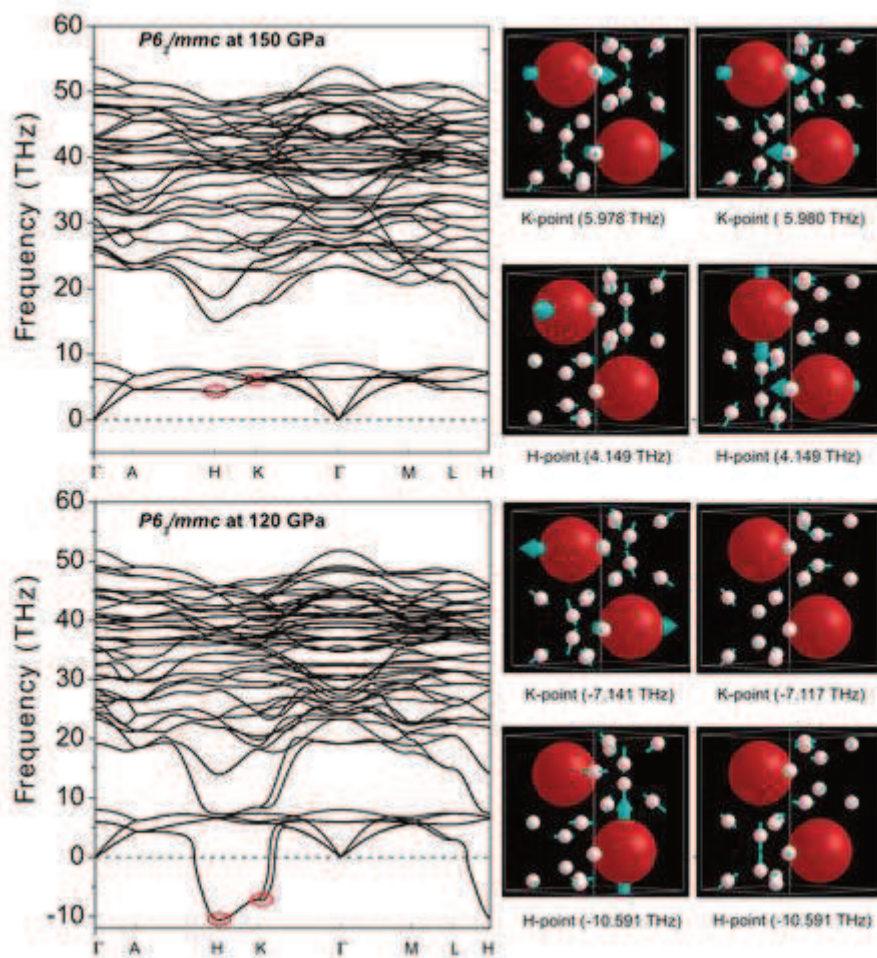
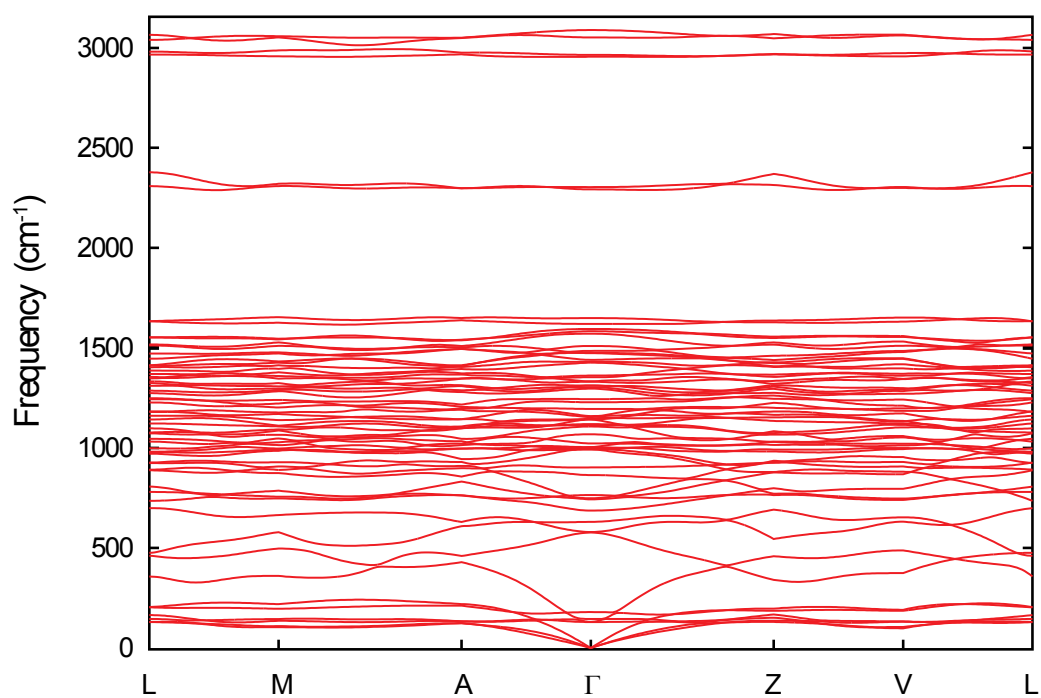


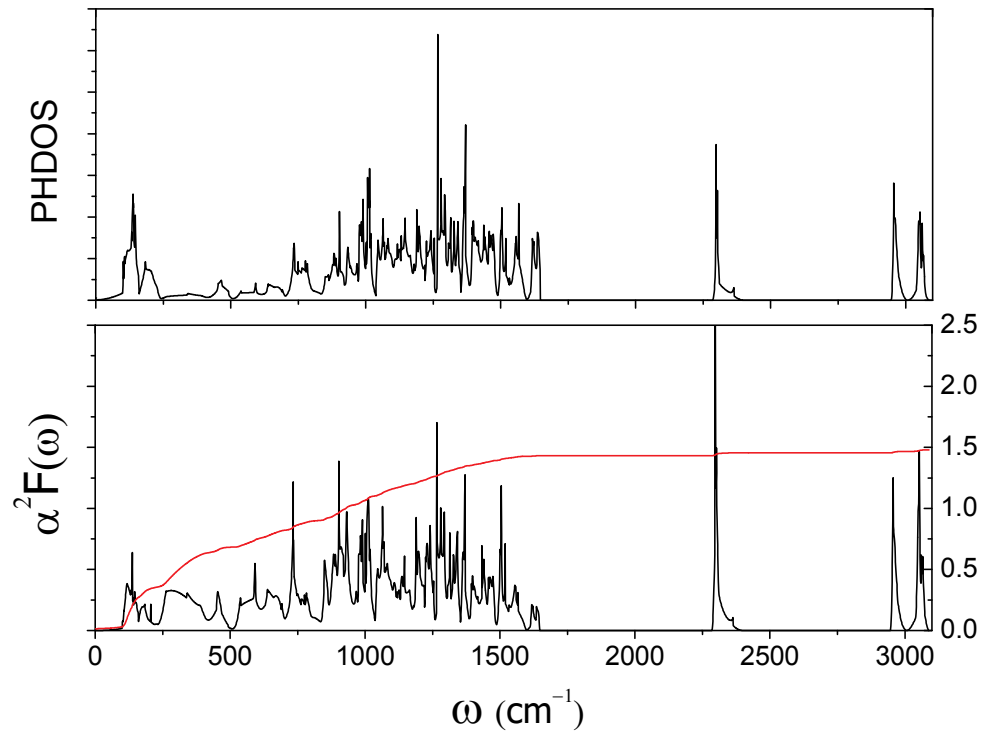
Figure S9: Electron localization function (ELF) of CeH₉ at 150 GPa. Figure (a), (b) and (c) represents ELF plots in (1.15 0 1), (1 1 0) and (-1 0 2.55) sections for CeH₉ at 150 GPa. Hydrogen atoms and H₄, H₅ and H₆ rings are shown in the figures. For better clarity, we set the minimum of the ELF to 0.2 in the plots.



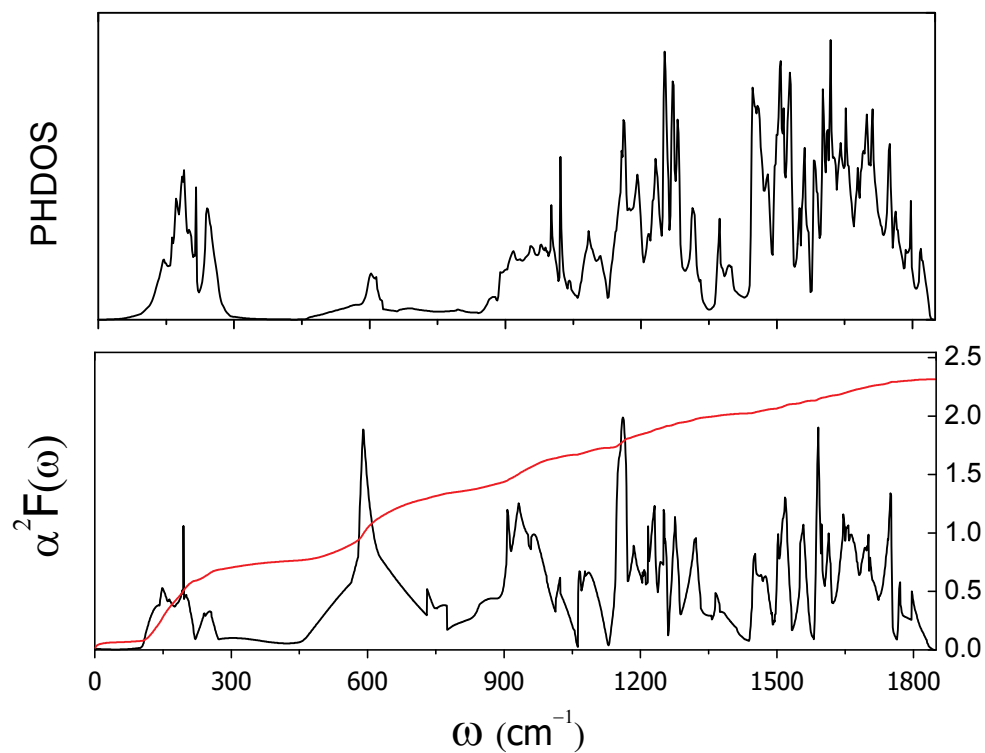
Supplementary Figure S10: Phonon dispersion curves and selected mode displacements of the $P6_3/mmc$ -CeH₉ at 120 and 150 GPa. Unstable modes i.e., H- and K-point can be seen at 120 GPa. Large and small spheres show Ce and H atoms, respectively. Arrows refer to the displacement direction.



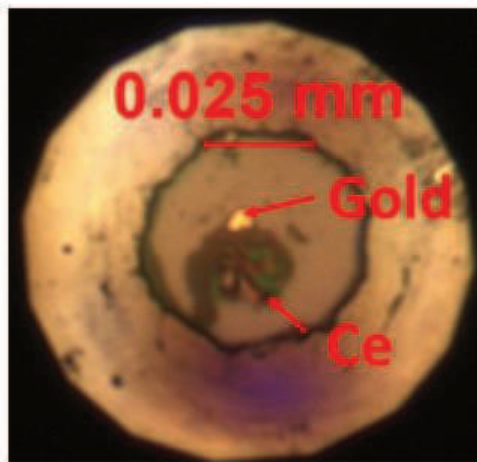
Supplementary Figure S11: Calculated phonon dispersion curves of $C2/c$ -CeH₉ at 100 GPa. Phonon calculations show that lower symmetry structure $C2/c$ does not have any imaginary frequency at 100 GPa, which simply refers to the stability of this phase. In addition to stability, lattice dynamics calculations show appearance of high frequency vibration of hydrogen atoms in the $C2/c$ phase.



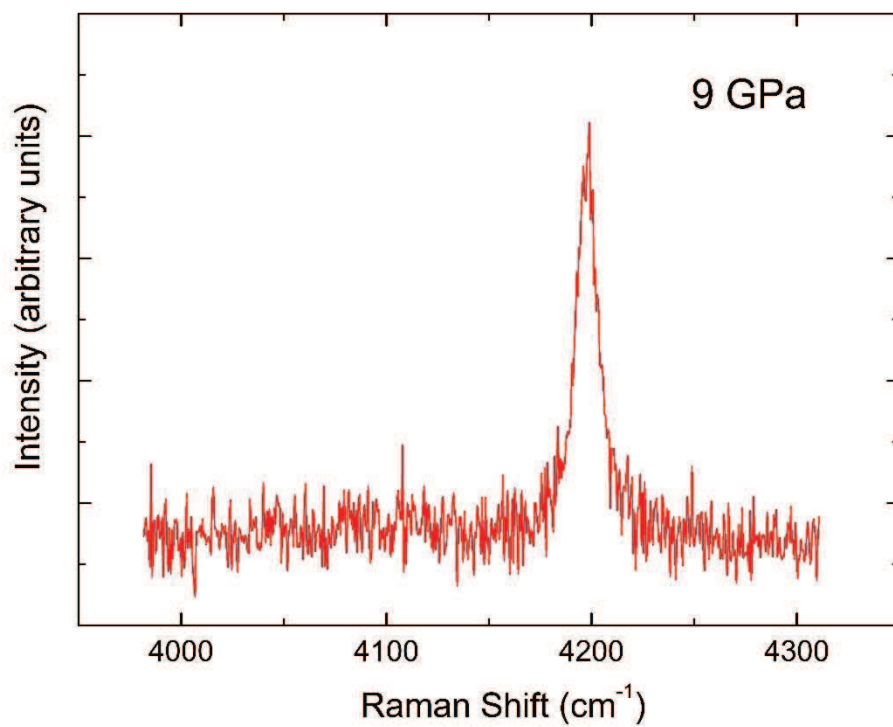
Supplementary Figure S12: (a) Calculated phonon density of states (PHDOS), (b) Eliashberg EPC spectral functions $\alpha^2F(\omega)$, and electron-phonon integral $\lambda(\omega)$ (red line) of $C2/c\text{-CeH}_9$, 100 GPa. Both phonon density of states and Eliashberg spectral function show a gap between medium-frequency and high-frequency vibration of H atoms. The electron-phonon coupling coefficient (red line) shows that medium-frequency H modes contribute the most to the electron-phonon coupling.



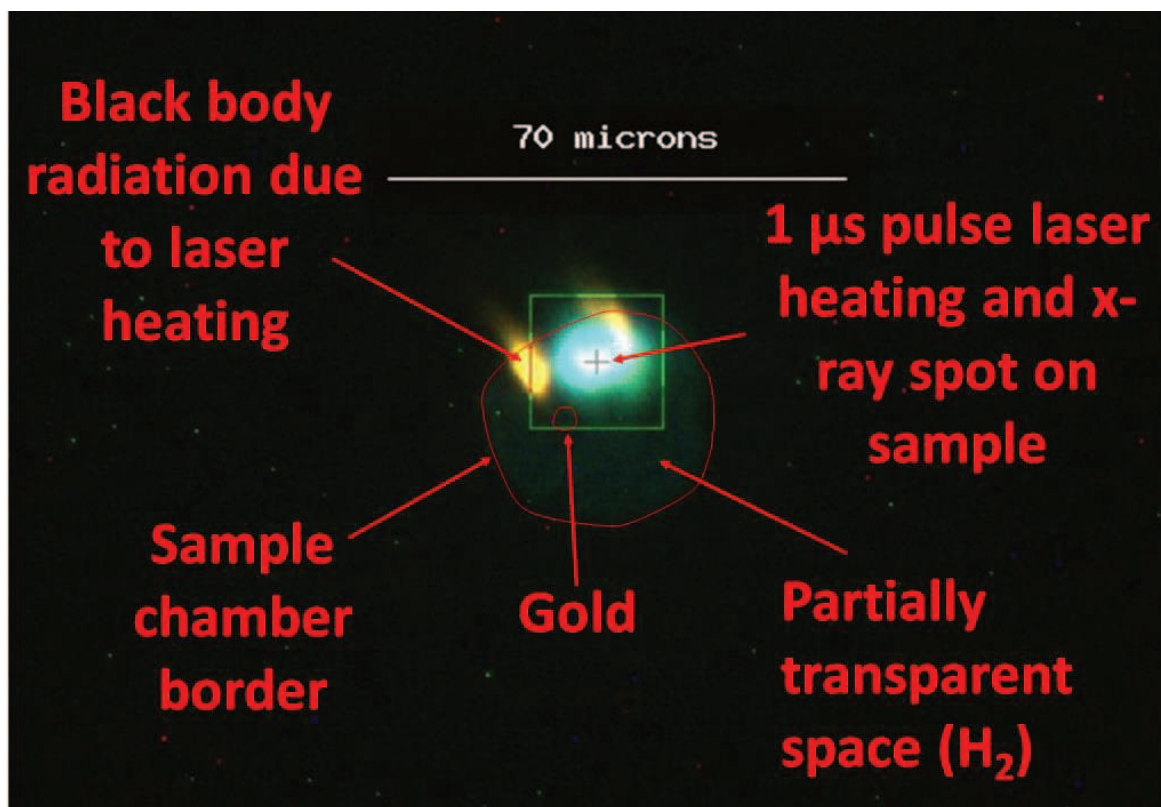
Supplementary Figure S13: (a) Calculated phonon density of states (PHDOS), (b) Eliashberg EPC spectral functions $\alpha^2F(\omega)$, and electron-phonon integral $\lambda(\omega)$ (red line) of $P6_3/mmc$ -CeH₉, 200 GPa. Contrary to the low-symmetry phase of CeH₉, $P6_3/mmc$ does not have hydrogen modes with frequency above 2000 cm⁻¹. The electron-phonon coupling coefficient (red line) shows that both medium-frequency and high-frequency H vibrations make a significant contribution to the electron-phonon coupling.



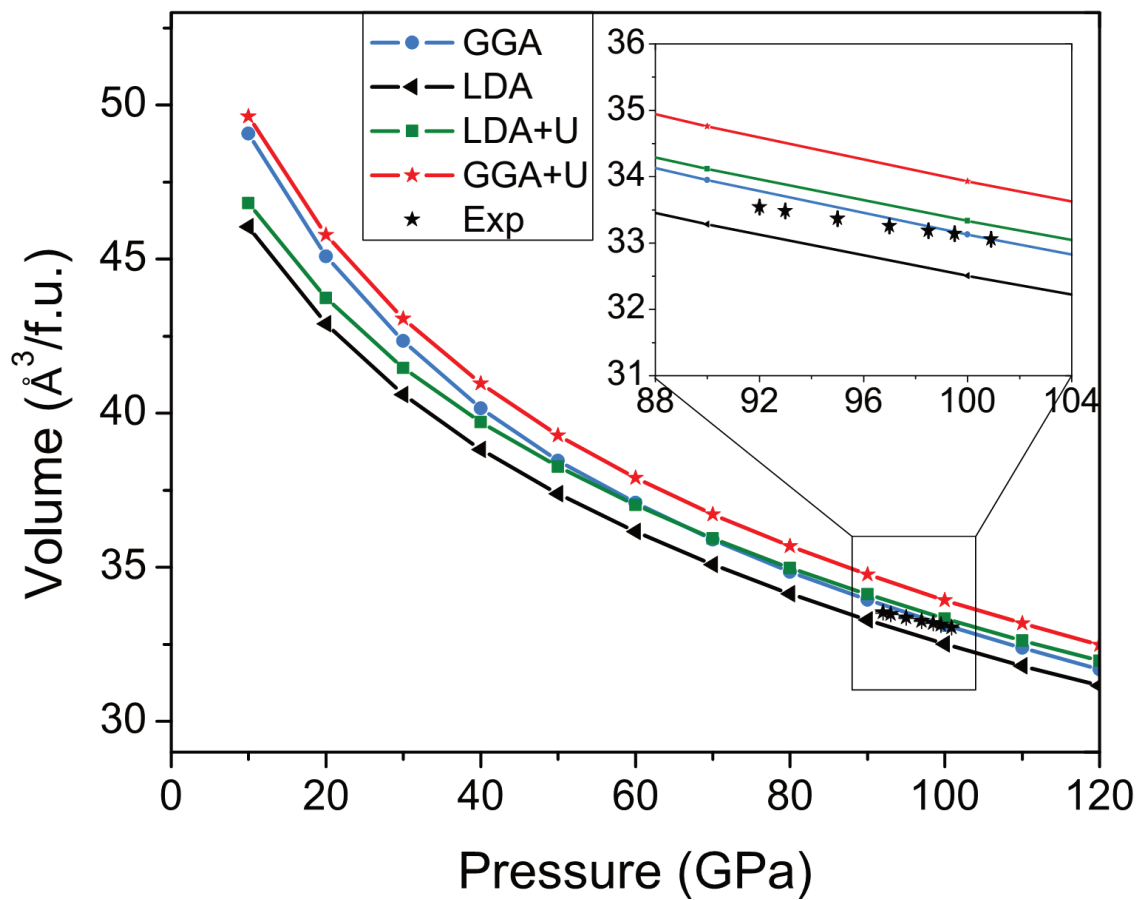
Supplementary Figure S14: Image of sample loading at 9 GPa. Image shows Ce (actually CeH_2) and Au surrounded by H_2 inside rhenium sample chamber at 9 GPa.



Supplementary Figure S15: Raman spectra recorded from sample chamber at 9 GPa. Raman spectra of H₂ vibron collected at 9 GPa from sample chamber confirming the presence of H₂ inside the sample chamber.



Supplementary Figure S16: Image of *in-situ* ~1 μs pulse laser heating and x-ray on sample at 100 GPa recorded at beamline 13-IDD of GSECARS at APS. Microsecond pulse laser heating of sample spot was always maintained at substantial distance from gasket corner (bright spot marked with an arrow) to avoid any unwanted reaction and contamination. Sample chamber edge and gold positions are marked with red line for clarity and labelled respectively in image. Partially transparent space shown with an arrow confirms the presence of hydrogen in sample chamber.



Supplementary Figure S17: Comparison of P-V data of various theoretical methods with experimental data.

Table S1: Crystal structures parameters of the predicted Ce-H phases.

Phase	Space group	Lattice Parameters	Atoms	<i>x</i>	<i>y</i>	<i>z</i>
CeH ₁₀ (200 GPa)	<i>Fm</i> $\bar{3}$ <i>m</i>	<i>a</i> = 4.877 Å	Ce (4a)	0.0000	0.0000	0.0000
			H (8c)	0.2500	0.2500	0.7500
			H (32f)	0.1227	0.1227	0.6227
CeH ₉ (200 GPa)	<i>P6</i> ₃ / <i>mmc</i>	<i>a</i> = 3.497 Å	Ce (2d)	0.6667	0.3333	0.2500
		<i>c</i> = 5.224 Å	H (12k)	0.1550	0.8450	0.4351
		H (4f)	0.3333	0.6667	0.1464	
H (2b)	0.0000	0.0000	0.7500			
CeH ₉ (100 GPa)	<i>C2/c</i>	<i>a</i> = 3.685 Å	Ce (4e)	0.5000	0.0823	0.2500
		<i>b</i> = 6.427 Å	H (8f)	0.9242	0.8255	0.4396
		<i>c</i> = 6.652 Å	H (8f)	0.5502	0.8258	0.0613
		<i>β</i> = 123.60°	H (8f)	0.8168	0.0862	0.0656
		H (8f)	0.1152	0.0840	0.8596	
H (4e)	0.0000	0.2482	0.2500			
CeH ₈ (80 GPa)	<i>P6</i> ₃ <i>mc</i>	<i>a</i> = 3.727 Å	Ce (2b)	0.6667	0.3333	0.7743
		<i>c</i> = 5.576 Å	H (2b)	0.6667	0.3333	0.1520
		H (6c)	0.1746	0.3492	0.9512	
		H (6c)	0.8434	0.6869	0.0910	
H (2a)	0.0000	0.0000	0.2745			
CeH ₆ (50 GPa)	<i>P6</i> ₃ <i>mc</i>	<i>a</i> = 3.704 Å	Ce (2b)	0.6667	0.3333	0.2894
		<i>c</i> = 5.733 Å	H (6c)	0.1778	0.3556	0.1077
		H (2a)	0.0000	0.0000	0.4456	
		H (2a)	0.0000	0.0000	0.7915	
H (2b)	0.3333	0.6667	0.4093			
CeH ₄ (50 GPa)	<i>I4/mmm</i>	<i>a</i> = 3.044 Å	Ce (2b)	0.5000	0.5000	0.0000
		<i>c</i> = 6.021 Å	H (4e)	0.0000	0.0000	0.8657
		H (4d)	0.0000	0.5000	0.2500	
CeH ₃ (50 GPa)	<i>Pm</i> $\bar{3}$ <i>n</i>	<i>a</i> = 3.815 Å	Ce (2a)	0.5000	0.5000	0.5000
			H (6d)	0.2500	0.5000	0.0000
CeH ₃ (0 GPa)	<i>Pm</i> $\bar{3}$ <i>n</i> (<i>β</i> -UH ₃ -type)	<i>a</i> = 6.570 Å	Ce (2a)	0.0000	0.0000	0.0000
			Ce (6c)	0.2500	0.0000	0.5000
			H (24k)	0.0000	0.1552	0.6953

Table S2: Comparison of electronic density of states of various hydrides

Hydride	Pressure (GPa)	N(E_f) (states/eV/f.u.)
<i>P6₃/mmc</i> -CeH ₉	100 GPa	0.918
<i>P6₃/mmc</i> -CeH ₉	150 GPa	0.812
<i>P6₃/mmc</i> -CeH ₉	200 GPa	0.732
<i>Im</i> $\bar{3}m$ -H ₃ S	200 GPa	0.525
<i>Fm</i> $\bar{3}m$ -LaH ₁₀	200 GPa	0.735

Table S3: Comparison of electron-phonon coupling coefficient (λ), logarithmic average phonon frequency (ω_{\log}) and T_c for various hydrides. (a)

Hydride	Space group	λ	ω_{\log} (K)	T_c (K)	Pressure (GPa)	reference
CeH ₉	$P6_3/mmc$	2.30	740	117	200	This study
CeH ₉	$C2/c$	1.48	662	75	100	This study
H ₃ S	$Im\bar{3}m$	2.19	1335	203	200	4
YH ₁₀	$Im\bar{3}m$	2.58	1282	326	250	5
LaH ₈	$C2/m$	1.12	1591	131	300	5
LaH ₁₀	$Fm\bar{3}m$	3.41	848	238	210	5
UH ₇	$P6_3/mmc$	0.83	873.8	47.6	20	6
		0.95	764.9	57.5	0	
UH ₈	$Fm\bar{3}m$	0.73	873.7	27.5	50	6
		1.13	450.3	37.6	0	
UH ₉	$P6_3/mmc$	0.67	933.4	35.8	300	6
AcH ₁₀	$R\bar{3}m$	3.46	710.9	204.1	200	7
AcH ₁₆	$P\bar{6}m2$	2.16	1054	199.2	150	7
ThH ₁₀	$Fm\bar{3}m$	2.19	1042.8	194.4	100	8

Table S4: Comparison of lattice parameters and volume of $P6_3/mmc$ -CeH₉ at 100 GPa by various DFT functionals

Functional	a (Å)	c (Å)	Vol (Å³/f.u.)
LDA	3.6827	5.5356	32.510
LDA+U (6 eV)	3.7072	5.6018	33.335
GGA	3.7022	5.5813	33.125
GGA+U (6 eV)	3.7259	5.6445	33.930
Experiment	3.7110	5.5429	33.053

Table S5: Comparison of bulk modulus of $P6_3/mmc$ -CeH₉ by various DFT functionals

Functional	bulk modulus K_0 (GPa)	V_0 (Å ³ /f.u.)	K_0'
LDA	98.1	49.9	4.0
LDA+U (6 eV)	105.4	50.4	4.0
GGA	80.5	53.4	4.0
GGA+U (6 eV)	84.4	54.0	4.0

References

- 1 Avisar, D. & Livneh, T. Raman scattering by phonons and crystal-field excitations in cerium hydrides. *Journal of Alloys and Compounds* **494**, 11-16, doi:<https://doi.org/10.1016/j.jallcom.2009.11.108> (2010).
- 2 Jacobsen, M. K., Velisavljevic, N., Dattelbaum, D. M., Chellappa, R. S. & Park, C. High pressure and temperature equation of state and spectroscopic study of CeO₂. *Journal of Physics: Condensed Matter* **28**, 155401 (2016).
- 3 Korst, W. L. & Warf, J. C. Rare Earth-Hydrogen Systems. I. Structural and Thermodynamic Properties. *Inorganic Chemistry* **5**, 1719-1726, doi:10.1021/ic50044a018 (1966).
- 4 Duan, D. *et al.* Pressure-induced metallization of dense (H₂S)₂H₂ with high-T_c superconductivity. *Scientific Reports* **4**, 6968, doi:10.1038/srep06968 (2014).
- 5 Liu, H., Naumov, I. I., Hoffmann, R., Ashcroft, N. W. & Hemley, R. J. Potential high T_c superconducting lanthanum and yttrium hydrides at high pressure. *Proceedings of the National Academy of Sciences* **114**, 6990-6995, doi:10.1073/pnas.1704505114 (2017).
- 6 Kruglov, I. A. *et al.* Uranium polyhydrides at moderate pressures: prediction, synthesis, and expected superconductivity. *arXiv:1708.05251* (2017).
- 7 Semenok, D. V., Kvashnin, A. G., Kruglov, I. A. & Oganov, A. R. Actinium Hydrides AcH₁₀, AcH₁₂, and AcH₁₆ as High-Temperature Conventional Superconductors. *The Journal of Physical Chemistry Letters*, 1920-1926, doi:10.1021/acs.jpcllett.8b00615 (2018).
- 8 Kvashnin, A. G., Semenok, D. V., Kruglov, I. A. & Oganov, A. R. High-Temperature Superconductivity in Th-H System at Pressure Conditions. *arXiv:1711.00278* (2017).